Inorg. Chem. **2006**, *45*, 10503–10519

Superstructure in $RE_{2-x}Fe_4Si_{14-y}$ (RE = Y, Gd–Lu) Characterized by Diffraction, Electron Microscopy, and Mössbauer Spectroscopy

Mi-Kyung Han,[§] Ya-Qiao Wu,[#] Matthew Kramer,[%,#] Benjamin Vatovez,[¶] Fernande Grandjean,[¶] Gary J. Long,*[,†] and Gordon J. Miller*[,§]

Department of Chemistry, Iowa State University, Ames, Iowa 50011, Department of Materials Science and Engineering, Iowa State University, Ames, Iowa 50011, Department of Chemistry, University of Missouri, Rolla, Missouri 65409-0010, and Department of Physics, B5 University of Liège, B-4000 Sart Tilman, Belgium

Received June 20, 2006

Ternary rare-earth iron silicides $RE_{2-x}Fe_4Si_{14-y}$ (RE = Y, Gd–Lu; $x \approx 0.8$; $y \approx 4.1$) crystallize in the hexagonal system with $a \approx 3.9$ Å, $c \approx 15.3$ Å, Pearson symbol *hP*20–4.9. Their structures involve rare-earth silicide planes with approximate compositions of "$RE_{1.2}Si_{1.9}$" alternating with β-$FeSi_2$-derived slabs and are part of a growing class of rare-earth/transition-metal/main-group compounds based on rare-earth/main-group element planes interspersed with (distorted) fluorite-type transition-metal/main-group element layers. The rare-earth silicide planes in the crystallographic unit cells show partial occupancies of both the RE and Si sites because of interatomic distance constraints. Transmission electron microscopy reveals a $4a \times 4b \times c$ superstructure for these compounds, whereas further X-ray diffraction experiments suggest ordering within the *ab* planes but disordered stacking along the *c* direction. A $4a \times 4b$ structural model for the rare-earth silicide plane is proposed, which provides good agreement with the electron microscopy results and creates two distinct Fe environments in a 15:1 ratio. Fe-57 Mössbauer spectra confirm these two different iron environments in the powder samples. Magnetic susceptibilities suggest weak (essentially no) magnetic coupling between rare-earth elements, and resistivity measurements indicate poor metallic behavior with a large residual resistivity at low temperatures, which is consistent with disorder. First-principles electronic-structure calculations on model structures identify a pseudogap in the densities of states for specific valence-electron counts that provides a basis for a useful electron-counting scheme for this class of rare-earth/transition-metal/main-group compounds.

Introduction

Ternary rare-earth iron silicides have attracted a great deal of attention recently because they form in a variety of crystal structures and exhibit a range of interesting properties,[1,2] such as superconductivity,[3] heavy-fermion behavior,[4,5] Kondo effects,[6] or valence fluctuations.[7,8] Therefore, these compounds provide the opportunity to improve our understanding of the many interesting physical properties arising from the interactions among the 4f electrons of the rare-earth elements, the 3d electrons of the Fe atoms, and the conduction electrons. Another related compound class gathering attention

* To whom correspondence should be addressed. E-mail: gmiller@iastate.edu (G.J.M.); glong@umr.edu (G.J.L.).
§ Department of Chemistry, Iowa State University.
# Materials and Engineering Physics Program, Ames Laboratory.
% Department of Materials Science and Engineering, Iowa State University.
† Department of Chemistry, University of Missouri, Rolla.
¶ Department of Physics, University of Liège.

(1) Rogl, P. In *Handbook of Physics and Chemistry of Rare Earths*; Gschneidner, K. A., Jr., Eyring, L., Eds.; Elsevier Science Publishers: Amsterdam, 1984; Vol. 7, p 1.
(2) Leciejewicz, J.; Szytula, A. In *Handbook of Physics and Chemistry of Rare Earths*; Gschneidner, K. A., Jr.; Eyring, L., Eds.; Elsevier Science Publishers: Amsterdam, 1989; Vol. 12, p 133.
(3) Cashion, J. D.; Shenoy, G. K.; Niarchos, D.; Viccaro, P. J.; Aldred, A. T.; Falco, C. M. *J. Appl. Phys.* **1981**, *52*, 2180.
(4) Li, H. S.; Coey, J. M. D. In *Handbook of Magnetic Materials*; Buschow, K. H. J., Ed.; Elsevier Science Publishers: Amsterdam, 1991; Vol. 6, p 1.
(5) Franse, J. J. M.; Radwanski, R. J. In *Handbook of Magnetic Materials*; Buschow, K. H. J., Ed.; Elsevier Science Publishers: Amsterdam, 1993; Vol. 7, p 307.
(6) Singh, Y.; Ramakrishnan, S.; Hossain, Z.; Geibel, C. *Phys. Rev. B* **2002**, *66* (1), 014415.
(7) Noguchi, S.; Okuda, K.; Abliz, M.; Goto, K.; Kindo, K.; Haga, Y.; Yamamoto, E.; Onuki, Y. *Phys. B* **1998**, *246*−*247*, 456.
(8) Gordon, R. A.; Warren, C. J.; Alexander, M. G.; Disalvo, F. J.; Pöttgen, R. *J. Alloys Compd.* **1997**, *248*, 27.

10.1021/ic061117c CCC: $33.50
Published on Web 11/29/2006

is the semiconducting silicides, especially those with a band gap smaller than that of silicon, because of their potential applications in the electronic and energy-conversion fields. β-Iron disilicide, a semiconductor with a direct gap of 0.79 eV,[9] has attracted considerable attention, so far, for solar cells and optoelectronic devices because of its compatibility with silicon technology, as well as the low-cost availability of the component elements.[10,11] Considerable effort has been devoted to modify the optical or transport properties of the semiconducting silicides, as well as to develop new alternative materials. Here, intermetallic compounds with high-silicon content offer an interesting possibility. Especially, when homogeneous ternary phases can be formed with an active metal and a transition metal, interesting optical, transport, and magnetic properties are expected.

At present, more than 100 rare-earth iron silicides are known, and they crystallize in more than 20 different crystal structures.[12] However, most of them have silicon contents no greater than 50 atomic percent, for example, $REFe_2Si_2$ with the $BaAl_4$-structure type[13] and $RE_2Fe_3Si_5$ with the $Sc_2Fe_3Si_5$-structure type.[14] During the course of our exploration and investigation of rare-earth transition-metal silicides for possible magnetocaloric effects, we prepared and characterized the $RE_{2-x}Fe_4Si_{14-y}$ compounds with the heavier, smaller rare-earth elements RE = Gd−Lu, including Y. These compounds have among the largest silicon content of known ternary silicides at ~66 atomic percent. From our X-ray diffraction studies, the $RE_{2-x}Fe_4Si_{14-y}$ compounds crystallize with the hexagonal $Sc_{1.2}Fe_4Si_{9.9}$ structure (a = 3.897(1) Å, c = 15.160(4) Å),[15] a structure which consists of $FeSi_2$ slabs alternating with RE−Si planes along the c axis. The RE−Si planes are especially interesting with respect to both structural and property implications because both atomic sites are partially occupied, which, as we discuss below, is demanded by distance criteria. Moreover, these structures are members of a growing family of rare-earth/transition-metal/Al or Ga structures involving rare-earth/Al or Ga planes alternating with fluorite-type transition-metal/Al or Ga layers.[16−22] Many of these structures exhibit an ordering of rare-earth and main-group metals in the planes to create orthorhombic or monoclinic "superstructures" of a hexagonal subcell. Among silicide examples, in addition to $Sc_{1.2}Fe_4Si_{9.9}$,[15] $RE_2Fe_4Si_9$ (RE = Y, Gd−Lu) have been reported to show weakly antiferromagnetically coupled rare-earth sites,[23] but the reported unit-cell parameters are quite close to those we find herein for the corresponding $RE_{2-x}Fe_4Si_{14-y}$. Finally, the magnetic properties of $Gd_{1.2}Fe_4Si_{9.8}$, $Er_{1.2}Fe_4Si_{9.8}$, and $U_{1.2}Fe_4Si_{9.8}$ have been studied because of their potential magnetic frustration.[24−27] In all of these reports, however, no observation was mentioned regarding any superstructure of the hexagonal unit cells.

In light of the potential superstructures that could be observed for $RE_{2-x}Fe_4Si_{14-y}$, as well as possible modifications of semiconducting β-$FeSi_2$, we report herein a thorough examination of the chemical composition and structure of $RE_{2-x}Fe_4Si_{14-y}$ (RE = Y, Gd−Lu) using a combination of electron microscopy and X-ray diffraction and demonstrate a new superstructure for this class of compound. We also report results from physical characterizations and the effectiveness of Mössbauer spectroscopy to assist with both chemical and structural characterization of these compounds. Finally, with the aid of first-principles electronic-structure calculations, a preliminary proposal for an electron-counting rule is presented to account for many examples in this class of rare-earth/transition-metal/main-group compounds.

Experimental Section

Synthesis. Rare-earth iron silicides of approximate compositions $RE_{1.2}Fe_4Si_{9.9}$ (RE = Y, Gd, Tb, Dy, Ho, Er, Tm, Yb, and Lu) were synthesized by arc-melting 0.5−0.7 g pellets of stoichiometric mixtures of the corresponding elements on a water-cooled copper hearth using a tungsten electrode in an atmosphere of ultrapure argon gas. The starting materials (rare-earth elements, Ames Lab Rare-Earth Metals Preparation Center, 99.99−99.9999%; Fe chips, Aldrich, 99.98%; Si pieces, Aldrich, 99.5%) were pre-arc-melted to remove impurities, such as oxygen, on the surfaces of the elements. During the arc-melting procedure, a titanium or zirconium pellet was heated prior to the melting of the reactant mixture to further purify the argon atmosphere. The samples were remelted after they were turned several times to promote homogeneity, and the weight losses during the arc-melting process were found to be less than 1−2 wt %. Attempts to anneal these products at 1273 K for 7 days led to the formation of secondary phases. All of these ternary silicides are stable with respect to decomposition or hydrolysis in air for long periods (more than 2 years) and show a silvery metallic luster.

Chemical Analysis. The chemical compositions of the products were analyzed by energy dispersive spectroscopy (EDS) quantitative analysis using a JEOL 8400A scanning electron microscope, equipped with an IXRF Systems iridium X-ray analyzer; the resulting compositions complemented the results from the single-crystal X-ray analysis. Typical data collections used a 20 kV accelerating voltage and a 30 nA beam current. To carry out both the qualitative and quantitative analyses, we used the following standards: elemental Fe and Si and, for the rare-earth elements,

(9) Giannini, C.; Lagomarsino, S.; Scarinci, F.; Castrucci, P. *Phys. Rev. B* **1992**, *45*, 8822.
(10) Bost, M. C.; Mahan, J. E. *J. Appl. Phys.* **1985**, *58*, 2696.
(11) Bost, M. C.; Mahan, J. E. *J. Appl. Phys.* **1988**, *64*, 2034.
(12) Villars, P.; Calvert, L. D. *Pearson's Handbook of Crystallographic Data for Intermetallic Phases*; ASM International: Materials Park, OH, 1997.
(13) Rossi, D.; Marazza, R.; Ferro, R. *J. Less-Common Met.* **1978**, *58*, 203.
(14) Braun, H. F. In *Ternary Superconductors*; Shenoy, G. K., Dunlap, B. D., Fradin, F., Eds.; Elsevier: NewYork, 1981; p 225.
(15) Kotur, B. Ya.; Bruvo, M. *Kristallografiya* **1991**, *36*, 1391.
(16) Gladyshevskii, R. E.; Strusievicz, O. R.; Cenzual, K.; Parthé, E. *Acta Crystallogr.* **1993**, *B49*, 474.
(17) Niermann, J.; Jeischko, W. *Z. Anorg. Allg. Chem.* **2002**, *628*, 2549.
(18) Zhuravleva, M. A.; Chen, X. Z.; Wang, X.; Schultz, A. J.; Ireland, J.; Kannewurf, C. K.; Kanatzidis, M. G. *Chem. Mater.* **2002**, *14*, 3066.
(19) Latturner, S. E.; Kanatzidis, M. G. *Inorg. Chem.* **2002**, *41*, 5479.
(20) Schlüter, M.; Jeitschko, W. *J. Solid State Chem.* **2003**, *172*, 27.
(21) Niermann, J.; Jeitschko, W. *Inorg. Chem.* **2004**, *43*, 3264.
(22) Niermann, J.; Jeischko, W. *Z. Anorg. Allg. Chem.* **2004**, *630*, 361.
(23) Gladyshevskij, E. I.; Bodak, O. I.; Jarovets, V. I.; Gorelenko, Ju. K.; Skolzdra, R. V. *Ukr. Fiz. Zh.* **1978**, *23*, 77.
(24) Noguchi, S.; Okuda, K.; Adachi, T.; Yoshida, T. *Phys. B* **1997**, *237*−*238*, 612.
(25) Noguchi, S.; Okuda, K.; Adachi, T.; Haga, Y.; Yamamoto, E.; Ônuki, Y. *J. Phys. Soc. Jpn.* **1997**, *66*, 2572.
(26) Noguchi, S.; Sakon, T.; Nojiri, H.; Motokawa, M. *Phys. B* **2004**, *346*−*347*, 179.
(27) Noguchi, S.; Sakon, T.; Nojiri, H.; Motokawa, M. *Phys. B* **2004**, *346*−*347*, 183.

YMn_2, RFe_2 (R = Gd, Dy), or R_2Fe_{17} (R = Tb, Ho, Er, Lu). The RE/Fe/Si ratios for all the products are in fairly good agreement with the results obtained from the refinements of single-crystal X-ray diffraction data (see subsequent section for results).

Microstructure Characterization. A Philips CM 30 transmission electron microscope (TEM) was employed for TEM/high-resolution TEM (HRTEM) investigations. The TEM was operated at 300 kV for microstructure characterization. TEM samples were prepared using the crush-float method.[28] Small pieces of alloys were crushed in a methanol solution using a mortar and pestel and then dropped onto a carbon-coated 3 mm Cu grid with lacey network support film from Ted Pella, Inc. The lacey support film contains holes varying in size from less than 0.25 μm to more than 10 μm, which is ideal for the specimens because the sizes of the crushed sample vary in the same range. The edges of the crushed small sample pieces can be as thin as 50 nm, which is ideal for TEM/HRTEM characterization. [0001] and [11$\bar{2}$0] orientations of the products are selected for TEM/HRTEM characterizations.

Structure Determination. The samples were characterized by single crystal and powder X-ray diffraction (XRD) at ambient temperature. The powder diffraction patterns were obtained with a Huber 670 image-plate camera equipped with monochromatic Cu Kα_1 radiation (λ = 1.540598 Å). Powdered samples were homogeneously dispersed on a Mylar film with the aid of a little petroleum jelly. The step size was set at 0.005°, and the exposure time was 1 h. Data acquisition was controlled via the in situ program. The lattice parameters of $RE_{2-x}Fe_4Si_{14-y}$ (RE = Y, Gd−Lu) were obtained from least-squares refinement of data in the range of 2θ between 10 and 90° with the aid of a Rietveld refinement program.[29]

Blocklike single crystals (typical crystal dimensions of 0.1−0.2 × 0.1−0.2 × 0.1−0.3 mm^3) were selected from the products and were mounted on glass fibers. These diffraction experiments used a Bruker *APEX* diffractometer equipped with monochromated Mo Kα radiation (λ = 0.71073 Å) and a detector-to-crystal distance of 5.990 cm. Diffraction data were collected at room temperature over a hemisphere or full sphere of reciprocal space with 0.3° scans in ω and with an exposure time of 10 s per frame up to 2θ = 56.55°. Intensities were extracted and then corrected for Lorentz and polarization effects using the *SAINT* program.[30] The program *SADABS* was used for empirical absorption correction.[31] Structure refinements (full-matrix least-squares on F^2) were performed using the *SHELXTL-PLUS* programs.[32]

Mössbauer Spectra. The Mössbauer spectra were measured at 85 and 295 K on a constant-acceleration spectrometer which used a rhodium-matrix cobalt-57 source and was calibrated at room temperature with α-iron foil. The Mössbauer spectral absorbers contained 3.5−7 mg/cm^2 of sample. The spectrum of $Gd_{1.2}Fe_4Si_{9.88}$ was also measured at 4.2 K with 14 mg/cm^2 of sample. The spectra have been fit with symmetric doublets as discussed below and the estimated relative errors are at most ±0.005 mm/s for the isomer shifts and ± 0.01 mm/s for the quadrupole splittings of the majority Fe site and the line widths, whereas the estimated relative errors are ±0.01 mm/s for the isomer shifts and ±0.02 mm/s for the quadrupole splittings of the minority Fe site. The absolute errors are approximately twice as large.

Electronic-Structure Calculations. The electronic structures of model $Y_{2-x}Fe_4Si_{14-y}$ structures were calculated self-consistently using the tight-binding linear muffin-tin-orbital (TB-LMTO) method within the atomic sphere approximation (ASA) using the LMTO, version 47, program.[33−36] Exchange and correlation were treated in a local spin-density approximation (LSDA).[37] All relativistic effects except spin−orbit coupling were taken into account using a scalar relativistic approximation.[38] Within the ASA, space is filled with overlapping Wigner−Seitz (WS) atomic spheres. The radii of the WS spheres were obtained by requiring the overlapping potential to be the best possible approximation to the full potential according to an automatic procedure.[36] Because these structures are not closely packed, empty spheres are also required to create an adequate potential. Two sets of empty spheres were generated: one near the RE−Si planes and the second within vacant cubes of the $FeSi_2$ layers. The WS radii for the atomic sites determined by this procedure are in the ranges of 1.93−2.00 Å for Y, 1.32−1.37 Å for Fe, and 1.35−1.44 Å for Si, depending upon the model and the atomic site in the corresponding asymmetric unit. The WS radii of all empty spheres ranged from 0.6 to 1.04 Å. The basis set included 5s, 5p, and 4d orbitals for Y, 4s, 4p, and 3d orbitals for Fe, 3s, 3p, and 3d orbitals for Si, and 1s and 2p orbitals for the empty spheres. The 3d orbitals of Si and the 2p orbitals of the empty spheres were treated with the Löwdin downfolding technique.[36] The reciprocal space integrations to determine the self-consistent charge density and densities of states (DOS) were performed by the tetrahedron method[39] using 50−100 *k* points in the irreducible wedges of the corresponding Brillouin zones for the models. The Fermi level was selected as the energetic reference level for each model.

Magnetic Measurements. DC magnetization data were collected using a Quantum Design MPMS (QD-MPMS) superconducting quantum interference device (SQUID) magnetometer with a 7 T superconducting magnet. Measurements were conducted on pieces of polycrystalline material (5−150 mg) in applied fields of 0.1−1 T at temperatures ranging from 1.85 to 300 K.

Resistance Measurements. The electrical resistance in zero field was measured with a Linear Research LR-700AC resistance bridge (f = 16 Hz, I = 1−3 mA) in the temperature environment of the same QD MPMS system, using a standard four-probe technique.

Results and Discussion

A series of polycrystalline rare-earth iron silicides $RE_{2-x}Fe_4Si_{14-y}$ (RE = Y, Gd−Lu), where x is ∼0.8 and y is ∼4.1 (i.e., $RE_{1.2}Fe_4Si_{9.9}$), has been prepared by arc melting. X-ray powder diffraction patterns showed single-phase products that could be assigned to the hexagonal $Sc_{1.2}Fe_4Si_{9.9}$ structure type (Pearson symbol *hP*20-4.9).[15] Scanning electron microscopy also confirmed single-phase products in most cases: both techniques did reveal occasional occurrences of either tetragonal α-$FeSi_2$ [40] (for Dy and Yb

(28) Williams, B. D.; Carter, B. *Transmission Electron Spectroscopy*; Plenum Press: New York, 1996.
(29) Hunter, B. A.; Howard, C. J. *Rietica*; Australian Nuclear Science and Technology Organization: Menai, Australia, 2000.
(30) *SMART*; Bruker AXS, Inc.; Madison, WI, 1996.
(31) Blessing, R. H. *Acta Crystallogr. A* **1995**, *A51*, 33.
(32) *SHELXTL*; Bruker AXS, Inc.: Madison, WI, 2000.
(33) Andersen, O. K. *Phys. Rev. B* **1975**, *12*, 3060.
(34) Andersen, O. K.; Jepsen, O. *Phys. Rev. Lett.* **1984**, *53*, 2571.
(35) Andersen, O. K.; Jepsen, O.; Glötzel, D. In *Highlights of Condensed-Matter Theory*; Bassani, F., Fumi, F., Tosi, M. P., Lambrecht, W. R. L., Eds.; North-Holland: New York, 1985.
(36) Andersen, O. K. *Phys. Rev. B* **1986**, *34*, 2439.
(37) Von Barth, U.; Hedin, L. *J. Phys. C* **1972**, *5*, 1629.
(38) Koelling, D. D.; Harmon, B. N. *J. Phys. C* **1977**, *10*, 3107.
(39) Blöchl, P. E.; Jepsen, O.; Andersen, O. K. *Phys. Rev. B* **1994**, *49*, 16223.
(40) Egert, B.; Panzner, G. *Phys. Rev. B* **1984**, *29*, 2091.

Table 1. Lattice Constants and Chemical Compositions for $RE_{1.2}Fe_4Si_{9.9}$ (RE = Y, Gd−Lu)[a]

XRD	SEM	*a* (Å)	*c* (Å)	*V* (Å^3)
$Y_{1.21(1)}Fe_4Si_{9.88(4)}$	$Y_{1.13(3)}Fe_4Si_{10.05(9)}$	3.9397(1)	15.3014(1)	205.678(2)
		3.928(5)	*15.44(1)*	*206.3(3)*
$Gd_{1.20(1)}Fe_4Si_{9.88(4)}$	$Gd_{1.13(3)}Fe_4Si_{9.65(6)}$	3.9557(1)	15.3194(3)	207.596(6)
		3.936(5)	*15.50(1)*	*208.0(3)*
$Tb_{1.25(1)}Fe_4Si_{9.85(5)}$	$Tb_{1.23(3)}Fe_4Si_{10.07(11)}$	3.9404(1)	15.3084(2)	205.845(4)
		3.943(5)	*15.48(1)*	*208.4(3)*
$Dy_{1.17(1)}Fe_4Si_{9.94(4)}$	$Dy_{1.12(5)}Fe_4Si_{9.56(7)}$	3.9370(1)	15.2913(2)	205.261(5)
		3.930(5)	*15.45(1)*	*206.7(3)*
$Ho_{1.16(1)}Fe_4Si_{9.86(4)}$	$Ho_{1.27(1)}Fe_4Si_{9.60(5)}$	3.9353(1)	15.2657(2)	204.740(5)
		3.924(5)	*15.43(1)*	*205.8(3)*
$Er_{1.05(1)}Fe_4Si_{9.90(4)}$	$Er_{1.23(7)}Fe_4Si_{9.94(17)}$	3.9326(1)	15.2873(2)	204.749(5)
		3.924(5)	*15.42(1)*	*205.6(3)*
$Tm_{1.21(1)}Fe_4Si_{9.90(5)}$		3.9280(1)	15.2483(4)	203.749(9)
		3.923(5)	*15.40(1)*	*205.3(3)*
$Yb_{1.07(1)}Fe_4Si_{9.91(4)}$		3.9225(1)	15.2696(3)	203.462(7)
		3.916(5)	*15.39(1)*	*204.4(3)*
$Lu_{1.21(1)}Fe_4Si_{9.78(4)}$	$Lu_{1.26(2)}Fe_4Si_{10.23(6)}$	3.9298(1)	15.2833(1)	204.404(2)
		3.910(5)	*15.39(1)*	*203.8(3)*

[a] Lattice constants are obtained from X-ray powder diffraction (T = 298 K, Cu Kα_1, $10° \le 2\theta \le 90°$). Those printed in *italics* are literature values for $RE_2Fe_4Si_9$.[23] Chemical compositions from SEM and refinement of single crystal X-ray diffraction are included.

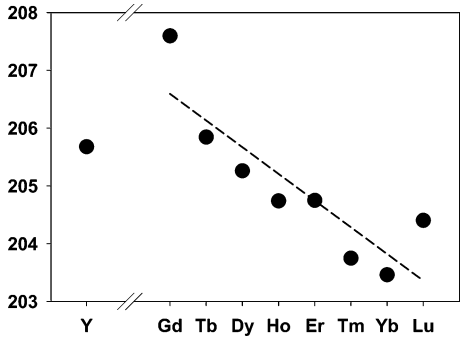

Figure 1. Trends in unit cell volumes with rare-earth element in $RE_{1.2}Fe_4Si_{9.9}$ (RE = Y, Gd−Lu).

cases) or $RE_2Fe_3Si_5$ [41] (Er case) as a secondary phase. Samples for subsequent characterizations, however, were checked for phase purity before further investigations. The lattice parameters from the X-ray powder diffraction experiments and chemical compositions obtained from both SEM and refinements of single-crystal X-ray diffraction are summarized in Table 1. Given our results, we will describe $RE_{2-x}Fe_4Si_{14-y}$ as $RE_{1.2}Fe_4Si_{9.9}$ for the remainder of this paper. For comparison, we also include the chemical compositions resulting from refinements of single-crystal X-ray diffraction data. As Table 1 points out, our unit-cell parameters are close to those reported for $RE_2Fe_4Si_9$,[23] but our measured *a* and *c* parameters are, respectively, systematically larger and smaller than these literature values. It is entirely possible that the reported $RE_2Fe_4Si_9$ phases[23] are, in fact, $RE_{1.2}Fe_4Si_{9.9}$.

A plot of the unit cell volumes versus atomic number of the RE atoms, shown in Figure 1, reflects the well-known lanthanide contraction and does not show any significant discontinuities. Somewhat surprising is the nonlinear behavior of the volumes with atomic number, but we also find irregular variation of the rare-earth element content. Nevertheless, according to these plots, Yb seems to behave like Yb^{3+}, which we address later with regard to measured physical properties. We could prepare this series only for the heavier lanthanides; the lighter lanthanides typically give mixtures of $REFe_2Si_2$- and $NaZn_{13}$-type or $ThMn_{12}$-type products.[42,43]

Structural Description. $RE_{1.2}Fe_4Si_{9.9}$ (RE = Y, Gd−Lu) crystallize in the hexagonal space group $P6_3/mmc$ (No. 194) at ambient temperature. Details of the single-crystal data collection parameters and crystallographic refinement results for these compounds are listed in Table 2. A comparison between unit-cell parameters obtained by X-ray single-crystal and those obtained powder diffraction patterns reveals generally good agreement, except for $Yb_{1.2}Fe_4Si_{9.9}$, a result which may suggest a different composition between well-formed single crystals and the powder for this particular system. However, these results were reproducible, and an explanation of their differences remains an open question. The atomic positions, site occupancies, and isotropic temperature displacement parameters are listed in Table 3. Selected interatomic distances are summarized in Table 4. The refined chemical compositions from single-crystal X-ray diffraction results are in good agreement with the compositions obtained by the SEM elemental analyses; these compositions are included in Table 1 for comparison.

Among the five crystallographic sites identified in the structure, only three refine as fully occupied: those for 4f Fe, 4f Si(1), and 4e Si(2), the atoms which form the $FeSi_2$ slabs. The other two sites in the asymmetric unit, 2d RE and 6h Si(3), respectively, are partially occupied by RE and Si atoms, and form planes at z = 1/4 and 3/4 in the crystallographic unit cell with approximate refined compositions $RE_{1.2}Si_{1.9}$. Full occupancy of these sites would lead to the crystal chemical formula $RE_2Fe_4Si_{14}$ in the unit cells, but the refined compositions achieve approximately $RE_{1.2}Fe_4Si_{9.9}$. In every case, the highest residual electron density is located at the site (1/3, 2/3, 1/4), with a value of ~0.875 e^-. These residual peaks listed in Table 2 range from 1.18 $e^-/Å^3$ for $Tm_{1.2}Fe_4Si_{9.9}$ to 2.67 $e^-/Å^3$ for $Yb_{1.2}Fe_4Si_{9.9}$. The next-highest residual electron density is located at different sites for each $RE_{1.2}Fe_4Si_{9.9}$ case throughout its corresponding

(41) Moodenbaugh, A. R.; Cox, D. E.; Vining, C. B.; Segre, C. U. *Phys. Rev. B* **1984**, *29*, 271.

Table 2. Crystallographic Data from Single-Crystal X-ray Diffraction Measurements for $RE_{1.2}Fe_4Si_{9.9}$ (RE = Y, Gd−Lu) at 300 K with Mo Kα Radiation

	Y	Gd	Tb	Dy	Ho	Er	Tm	Yb	Lu
a (Å)	3.9408(6)	3.9516(6)	3.9352(6)	3.9348(6)	3.9371(6)	3.9390(6)	3.9256(6)	3.9493(6)	3.9225(6)
c (Å)	15.302(3)	15.342(3)	15.299(3)	15.268(3)	15.292(3)	15.276(3)	15.263(3)	15.327(3)	15.249(3)
V (Å^3)	205.79(6)	207.47(6)	205.17(6)	204.72(6)	205.28(6)	205.27(6)	203.70(6)	207.03(6)	203.19(6)
Z	1	1	1	1	1	1	1	1	1
abs coeff (mm^{-1})	16.613	17.636	18.476	19.104	19.695	20.397	21.261	21.615	22.791
F(000)	289	319	321	322	323	324	325	327	328
$2\theta_{max}$ (deg)	55.88	55.7	55.96	55.96	55.9	55.9	56.1	55.74	56.16
h, *k*, *l*	±4, ±4, ±19	±4, ±4, ±19	±3, ±4, ±18	±5, ±4, ±19	±4, ±5, ±19	±5, ±5, ±18	±5, ±5, ±19	±5, ±5, ±19	±4, ±4, ±19
reflns	1056	1118	1146	1536	1118	1546	1594	1557	1523
independent reflns	126	128	126	125	126	127	127	127	127
R(int)	0.0588	0.0178	0.0278	0.0278	0.0374	0.0334	0.0255	0.0354	0.0357
data/params	126/19	128/20	126/19	125/19	126/19	127/19	127/20	127/19	127/19
GOF (F^2)	1.199	1.215	1.297	1.182	1.351	1.192	1.197	1.220	1.193
R1 [$I > 2\sigma(I)$]	0.0208	0.0185	0.0185	0.0156	0.0176	0.0147	0.0169	0.0187	0.0167
wR2	0.0502	00415	0.0480	0.0317	0.0348	0.0313	0.0394	0.0472	0.0382
extinction coeff	0.041(5)	0.011(2)	0.030(4)	0.014(1)	0.017(5)	0.011(2)	0.043(3)	0.021(3)	0.017(2)
residual peaks (e$^-$/Å^3)	2.47/−0.66	1.88/−0.52	1.72/−0.91	1.75/−0.34	1.78/−0.50	1.67/−0.47	1.18/−0.59	2.67/−0.81	2.29/−0.90

Table 3. Site Occupancies, Atomic Coordinates and Equivalent Isotropic Displacement Parameters (Å^2) for $RE_{1.2}Fe_4Si_{9.9}$ (RE = Y, Gd−Lu)

compound	atom	Wyckoff site	occupancy	*x*	*y*	*z*	*U*(eq)
$Y_{1.21(1)}Fe_4Si_{9.88(4)}$	Y	2*d*	0.607(5)	2/3	1/3	1/4	6(1)
	Fe	4*f*	1	1/3	2/3	0.3925(1)	5(1)
	Si(1)	4*f*	1	2/3	1/3	0.4543(1)	6(1)
	Si(2)	4*e*	1	0	0	0.6325(1)	7(1)
	Si(3)	6*h*	0.314(6)	0.0668(14)	0.5329(7)	1/4	15(1)
$Gd_{1.20(1)}Fe_4Si_{9.88(4)}$	Gd	2*d*	0.598(3)	2/3	1/3	1/4	7(1)
	Fe	4*f*	1	1/3	2/3	0.3928(1)	7(1)
	Si(1)	4*f*	1	2/3	1/3	0.4546(1)	7(1)
	Si(2)	4*e*	1	0	0	0.6320(1)	9(1)
	Si(3)	6*h*	0.314(7)	0.0626(17)	0.5313(9)	1/4	15(2)
$Tb_{1.25(1)}Fe_4Si_{9.85(5)}$	Tb	2*d*	0.624(3)	2/3	1/3	1/4	6(1)
	Fe	4*f*	1	1/3	2/3	0.3923(1)	6(1)
	Si(1)	4*f*	1	2/3	1/3	0.4544(1)	7(1)
	Si(2)	4*e*	1	0	0	0.6332(1)	8(1)
	Si(3)	6*h*	0.308(7)	0.0670(17)	0.5335(9)	1/4	14(2)
$Dy_{1.17(1)}Fe_4Si_{9.94(4)}$	Dy	2*d*	0.583(3)	2/3	1/3	1/4	6(1)
	Fe	4*f*	1	1/3	2/3	0.3925(1)	6(1)
	Si(1)	4*f*	1	2/3	1/3	0.4544(1)	7(1)
	Si(2)	4*e*	1	0	0	0.6330(1)	8(1)
	Si(3)	6*h*	0.323(6)	0.0652(14)	0.5326(8)	1/4	16(2)
$Ho_{1.16(1)}Fe_4Si_{9.86(4)}$	Ho	2*d*	0.582(3)	2/3	1/3	1/4	6(1)
	Fe	4*f*	1	1/3	2/3	0.3927(1)	6(1)
	Si(1)	4*f*	1	2/3	1/3	0.4545(1)	6(1)
	Si(2)	4*e*	1	0	0	0.6326(1)	7(1)
	Si(3)	6*h*	0.310(6)	0.0658(16)	0.5329(8)	1/4	14(2)
$Er_{1.05(1)}Fe_4Si_{9.90(4)}$	Er	2*d*	0.527(2)	2/3	1/3	1/4	7(1)
	Fe	4*f*	1	1/3	2/3	0.3922(1)	6(1)
	Si(1)	4*f*	1	2/3	1/3	0.4544(1)	7(1)
	Si(2)	4*e*	1	0	0	0.6330(1)	8(1)
	Si(3)	6*h*	0.316(5)	0.0711(13)	0.5356(7)	1/4	15(1)
$Tm_{1.21(1)}Fe_4Si_{9.90(5)}$	Tm	2*d*	0.603(3)	2/3	1/3	1/4	7(1)
	Fe	4*f*	1	1/3	2/3	0.3921(1)	6(1)
	Si(1)	4*f*	1	2/3	1/3	0.4545(1)	7(1)
	Si(2)	4*e*	1	0	0	0.6340(1)	8(1)
	Si(3)	6*h*	0.316(7)	0.0694(18)	0.5347(9)	1/4	16(2)
$Yb_{1.07(1)}Fe_4Si_{9.91(4)}$	Yb	2*d*	0.535(3)	2/3	1/3	1/4	7(1)
	Fe	4*f*	1	1/3	2/3	0.3928(1)	6(1)
	Si(1)	4*f*	1	2/3	1/3	0.4546(1)	7(1)
	Si(2)	4*e*	1	0	0	0.6319(1)	8(1)
	Si(3)	6*h*	0.319(7)	0.0618(16)	0.5309(8)	1/4	16(2)
$Lu_{1.21(1)}Fe_4Si_{9.78(4)}$	Lu	2*d*	0.605(3)	2/3	1/3	1/4	7(1)
	Fe	4*f*	1	1/3	2/3	0.3918(1)	6(1)
	Si(1)	4*f*	1	2/3	1/3	0.4544(1)	7(1)
	Si(2)	4*e*	1	0	0	0.6344(1)	7(1)
	Si(3)	6*h*	0.296(7)	0.0692(15)	0.5346(8)	1/4	11(2)

unit cell. We return to the significance of this residual electron density in a subsequent section.

Figure 2 shows a (010) projection of the refined crystal structure of $RE_{1.2}Fe_4Si_{9.9}$ to highlight the two structural

Table 4. Selected Interatomic Distances (Å) in $RE_{1.2}Fe_4Si_{9.9}$, (RE = Y, Gd−Lu)

	Y	Gd	Tb	Dy	Ho	Er	Tm	Yb	Lu
RE−Fe	3.151(1)	3.163(1)	3.147(1)	3.145(1)	3.151(1)	3.145(1)	3.136(1)	3.161(1)	3.131(1)
RE−Si(2)	2.899(1)	2.912(1)	2.890(1)	2.890(1)	2.896(1)	2.892(1)	2.876(1)	2.913(1)	2.870(1)
RE−Si(3)	2.844(4)	2.860(4)	2.837(4)	2.841(4)	2.841(4)	2.829(3)	2.824(4)	2.860(4)	2.822(4)
	1.362(5)	1.355(6)	1.364(6)	1.358(6)	1.361(6)	1.380(5)	1.369(6)	1.351(5)	1.367(5)
Fe−Si(1)	2.464(2)	2.471(1)	2.462(1)	2.461(1)	2.462(1)	2.465(1)	2.458(1)	2.469(1)	2.457(1)
	2.344(2)	2.342(2)	2.345(2)	2.337(2)	2.337(2)	2.343(2)	2.343(2)	2.339(2)	2.345(2)
Fe−Si(2)	2.307(1)	2.313(1)	2.306(1)	2.305(1)	2.306(1)	2.307(1)	2.301(1)	2.312(1)	2.300(1)
Fe−Si(3)	2.364(2)	2.379(3)	2.359(2)	2.360(2)	2.365(2)	2.350(2)	2.347(3)	2.378(2)	2.341(2)
Si(1)−Si(1)	2.670(2)	2.673(2)	2.666(2)	2.664(2)	2.666(2)	2.667(2)	2.659(2)	2.672(2)	2.658(2)
Si(1)−Si(2)	2.635(1)	2.640(1)	2.638(2)	2.635(1)	2.635(1)	2.638(1)	2.638(1)	2.637(1)	2.638(1)
Si(2)−Si(3)	2.676(1)	2.688(1)	2.667(2)	2.667(1)	2.673(1)	2.670(1)	2.654(1)	2.687(1)	2.648(1)
Si(3)−Si(3)	2.360(8)	2.347(10)	2.363(10)	2.352(9)	2.357(10)	2.390(8)	2.371(11)	2.340(9)	2.368(9)
	1.581(8)	1.605(10)	1.572(10)	1.583(9)	1.580(10)	1.549(8)	1.554(11)	1.609(9)	1.554(9)

components: the $FeSi_2$ slabs and RE−Si(3) planes that alternate along the *c* axis. Chemical bonding within and between these building blocks must be of similar strength, on the basis of the numbers and values of the interatomic distances, so that these compounds truly form three-dimensional bonding networks. Furthermore, partial occupancy of atomic sites in the RE−Si(3) planes is required because of the interatomic distances (see Table 4 and subsequent discussion).

$FeSi_2$ Layers. Figure 3 illustrates the $FeSi_2$ structural motif found in this series of compounds and compares it with that of β-$FeSi_2$. Because of the hexagonal symmetry, the arrangement of Fe atoms in the (001) planes of $RE_{1.2}Fe_4Si_{9.9}$ are regular triangular (3^6) nets with long Fe−Fe separations of ~3.9 Å, an arrangement that differs from the (111) projection of Fe-atom planes in orthorhombic β-$FeSi_2$ because of the existence of some short Fe−Fe contacts of 2.97 Å. The structure of β-$FeSi_2$ is a distortion of a possible cubic fluorite-type γ-$FeSi_2$, which has been reported as a thin film.[44] The distortion from γ- to β-$FeSi_2$ involves shifts of both Fe and Si sites, which destroys the cubic symmetry and all 3-fold axes so that (111) Fe planes are irregular 3^6 nets. Nevertheless, in both β-$FeSi_2$ and $RE_{1.2}Fe_4Si_{9.9}$, the Fe atoms are coordinated by highly distorted cubes of Si atoms, which share edges to create the two-dimensional $FeSi_2$ slabs in $RE_{1.2}Fe_4Si_{9.9}$ or the three-dimensional network in β-$FeSi_2$. In $RE_{1.2}Fe_4Si_{9.9}$, seven of the eight nearest Si neighbors to Fe come from the $FeSi_2$ layers (i.e., the 4f Si(1) and 4e Si(2) sites), whereas the eighth neighbor comes from the partially occupied 6h Si(3) sites in the RE−Si(3) planes. The Fe−Si and Si−Si nearest-neighbor distances found in $RE_{1.2}Fe_4Si_{9.9}$ are, respectively, 2.30−2.47 and 2.34−2.68 Å, and

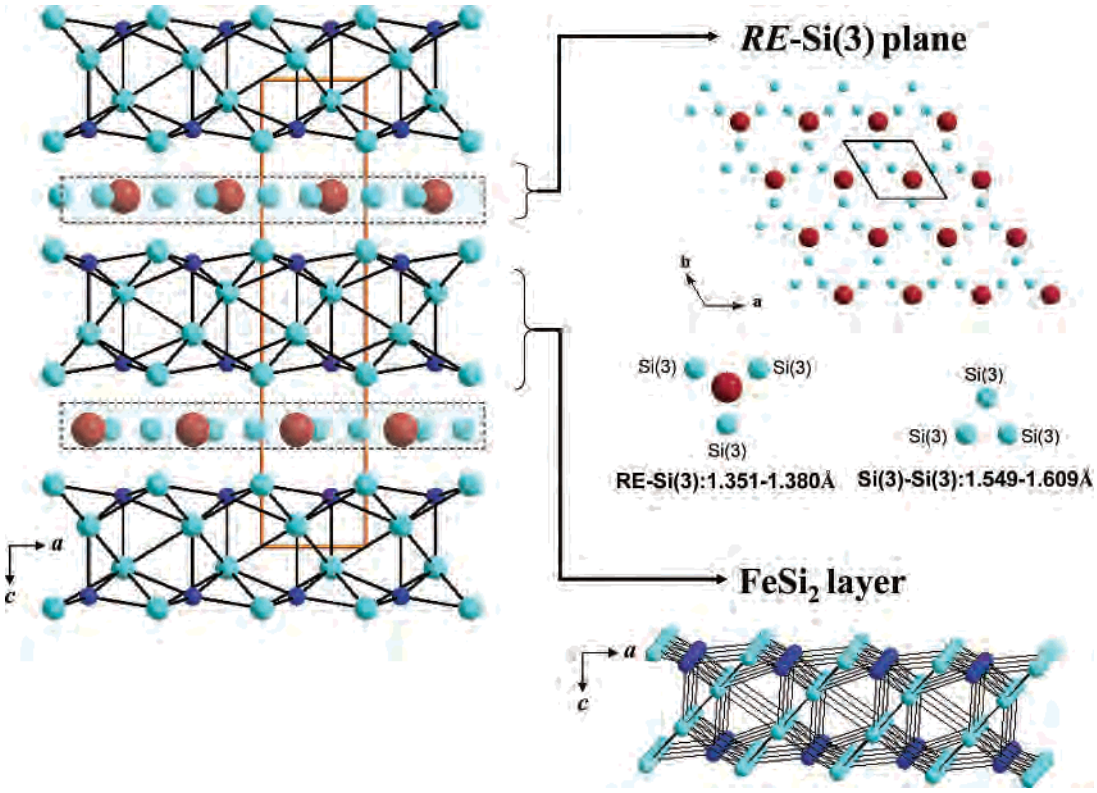

Figure 2. (left) Crystal structure of $RE_{1.2}Fe_4Si_{9.9}$ viewed perpendicular to the *b* axis. The unit cell is indicated. (upper right) RE−Si(3) plane viewed along the *c* axis, highlighting the short RE−Si(3) and Si(3)−Si(3) distances between the refined sites. (lower right) $FeSi_2$ layer viewed along the *b* axis. (RE, red spheres; Fe, blue spheres; Si, light-blue spheres.)

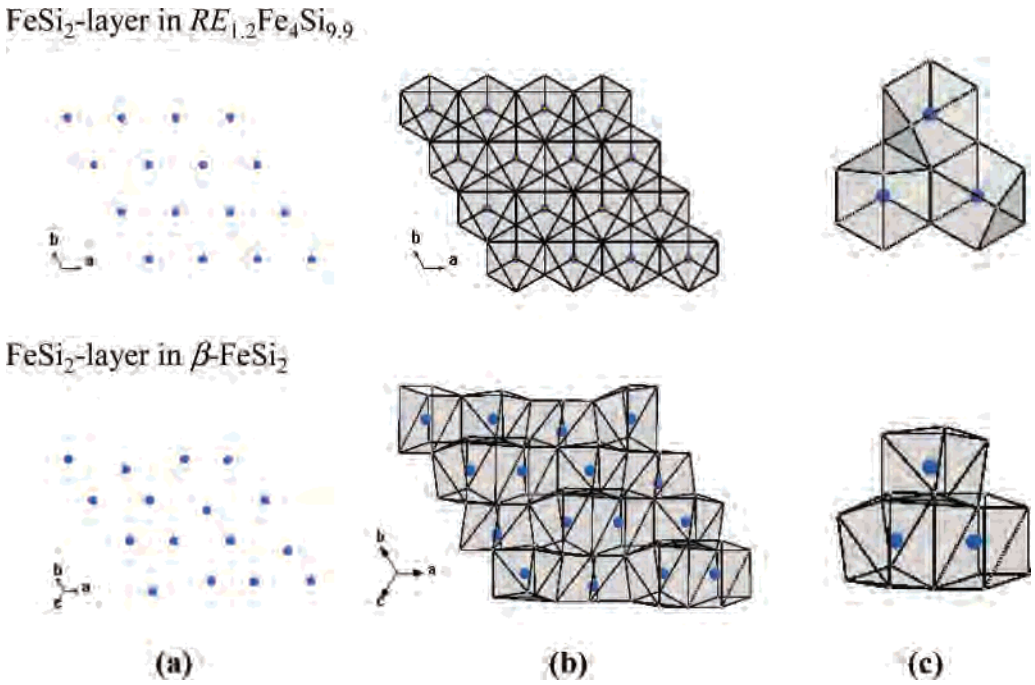

Figure 3. Comparison of $FeSi_2$ layer in $RE_{1.2}Fe_4Si_{9.9}$ with β-$FeSi_2$. (a) The arrangement of Fe atoms in (001) and (111) planes, respectively, for $RE_{1.2}Fe_4Si_{9.9}$ and β-$FeSi_2$, (b) the layers in panel a including the coordination polyhedra of Si neighbors, and (c) a magnification of three nearest-neighbor Fe atoms and the Si coordination.

match well to those found in β-$FeSi_2$ (i.e., 2.33−2.44 and 2.45−2.59 Å, respectively). In addition, these observed distances correlate well with the sum of the covalent radius of Si (1.18 Å) and the metallic radius for 12-coordinate Fe (1.26 Å).[45]

RE−Si(3) Planes. The 2d RE sites and the 6h Si(3) sites form atomic planes with the triangular pattern shown in Figure 2. Both sites are necessarily partially occupied because simultaneous occupation of every RE and Si(3) site in these layers would create physically unacceptable RE−Si(3) distances (i.e., 1.351(5)−1.380(5) Å for *RE*-Si(3) and 1.549(8)−1.609(9) Å for Si(3)−Si(3)). Consequently, the occupancies of the RE and Si(3) sites refine to approximately 60% at the 2d RE site (52.7(2)−62.4(3)%) and 31% at the 6h Si(3) site (29.6(7)−32.3(6)%) to give an approximate composition of $RE_{1.2}Si_{1.9}$. It is tempting to approximate these occupancies as 66.7% at the 2d RE site and 33.3% at the 6h Si(3), which would result in the composition "$RE_{1.33}Si_{2.00}$." However, this assignment significantly overestimates the composition of rare-earth elements determined in all cases, both by SEM analysis and by refinement of single-crystal X-ray diffraction data. Such intrinsically "disordered" planes of rare-earth and main-group elements (M = Al, Ga, Si, Ge) have been reported for a number of related compounds (e.g., $Ce_2Pt_6Ga_{15}$,[46] $A_2Pt_6Al_{15}$ (A = Y, Gd−Tm, Zr),[22] $RE_{0.67}Ni_2Ga_{5+n-x}Tt_x$ (RE = Y, Sm, Gd−Tm; Tt = Si, Ge; n = 0, 1),[18] $Gd_{0.67}Pt_2(Al, Si)_5$ and $Gd_{1.33}Pt_3(Al, Si)_8$,[19] and $RENi_3Al_9$ (RE = Y, Gd, Dy, Er)).[47] In each of these examples, the crystallographic unit cell is either hexagonal or rhombohedral and contains $RE(M)_3$ planes that exhibit similar partial occupancies to the RE−Si(3) planes in $RE_{1.2}Fe_4Si_{9.9}$. A survey of the crystallographic results from both X-ray and neutron diffraction experiments among these various examples shows extensive scattering of the site occupation factors for the 2d RE and 6h M sites, respectively, around 66.7 and 33.3%. One example, $Zr_{1.00(1)}Pt_4Al_{10.322(3)}$, has the 2d RE nearly 50% occupied (by Zr) and the 6h Al site (labeled Al(1) in the literature) 37% occupied.[22] Furthermore, some examples among $RE_{0.67}Ni_2Ga_{5-x}Tt_x$ also show occupations of the 2*d RE* site as significantly less than 66.7% occupied.[18] There remains at present no chemical understanding of these variations in composition for these different systems.

***4a* × *4b* Superstructure in the RE-Si(3) Plane.** The intrinsic fractional occupancy of the RE and Si(3) sites in all $RE_{1.2}Fe_4Si_{9.9}$ suggests that the unit cell found by X-ray diffraction is most likely a subcell of the true unit cell and that a superstructure with ordered RE and Si(3) sites may exist. This hypothesis is strongly suggested by the number of rare-earth/transition-metal/main-group examples that already show orthorhombic, monoclinic, or triclinic symmetry because of the ordering in the RE−M planes, as seen for example in $Y_2Co_3Ga_9$,[48] $RE_2Pt_9Ge_3$ (note that the role of transition-metal (Pt) and main-group element (Ge) is switched

(42) Sakurada, S.; Tsutai, A.; Sahashi, M. *J. Alloys Compd.* **1992**, *187*, 67.
(43) Han, M.-K. Ph.D. Thesis. Iowa State University, Ames, IA, 2006.
(44) Vazquez de Parga, A. L.; De La Figuera, J.; Ocal, C.; Miranda, R. *Europhys. Lett.* **1992**, *18*, 595.
(45) Huheey, J. E.; Keiter, E. A.; Keiter, R. L. *Inorganic Chemistry: Principles of Structure and Reactivity*, 4th ed.; Harper Collins College Publishers: New York; 1993; p 292.
(46) Kwei, G. H.; Lawson, A. C.; Larson, A. C.; Morosin, B.; Larson, E. M.; Canfield, P. C. *Acta Crystallogr.* **1996**, *B52*, 580.
(47) Gladyshevskii, R. E.; Cenzual, K.; Flack, H. D.; Parthé, E. *Acta Crystallogr.* **1993**, *B49*, 468.
(48) Grin, Yu. N.; Gladyshevsky, R. E.; Sichevich, O. M.; Zavodnik, V. E.; Yarmolyuk, Ya. P.; Rozhdestvenskaya, I. V. *Sov. Phys. Crystallogr.* **1984**, *29*, 528.

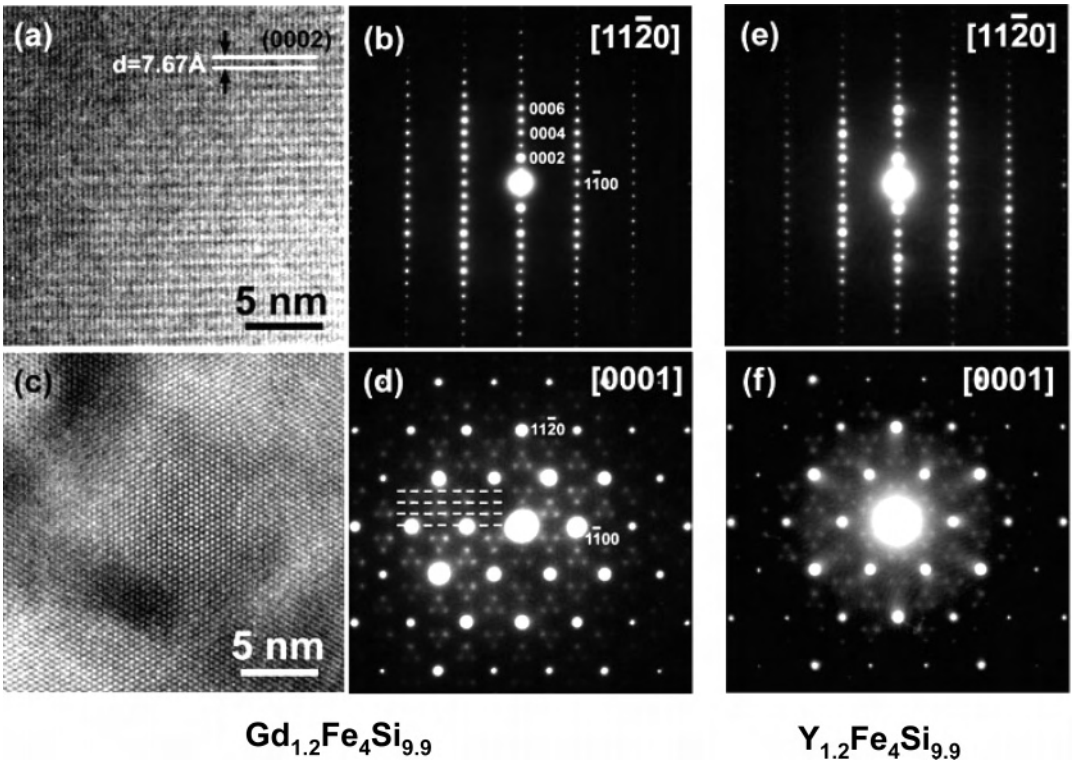

Figure 4. (left) HRTEM images of $Gd_{1.2}Fe_4Si_{9.9}$ oriented along (a) [11$\bar{2}$0] and (b) [0001]. (middle) SAEDPs of $Gd_{1.2}Fe_4Si_{9.9}$ oriented along (c) [11$\bar{2}$0] and (d) [0001]. (right) SAEDPs of $Y_{1.2}Fe_4Si_{9.9}$ oriented along (e) [11$\bar{2}$0] and (f) [0001].

in these examples),[49] $RE_4Pd_9Al_{24}$,[50] and $RE_4Pt_9Al_{24}$.[50] For these structures, the RE−M planes refine as precisely stoichiometric RE_2M_3 with 1/3 of the RE sites replaced by M_3 triangles in an ordered arrangement. Within just the two-dimensionally ordered RE_2M_3 plane, the unit cell becomes a $\sqrt{3}a \times \sqrt{3}b$ supercell of the smaller hexagonal cell. However, because of the stacking of these planes along the *c* axis, the hexagonal or trigonal symmetry is broken, and these structures adopt orthorhombic, monoclinic, or triclinic crystal classes.[48−50] There are examples, however, where a supercell remains unsolved because of the presence of diffuse scattering along the *c** direction. Kwei et al.[45] suggested a $3a \times 3b$ supercell for $Ce_2Pt_6Ga_{15}$ because of columns of diffuse scattering along *c** at $h \pm 1/3$, $k \pm 1/3$ in single-crystal neutron diffraction patterns, although the arrangement of atoms proposed for the $Ce(Ga)_3$ planes corresponds to the $\sqrt{3}a \times \sqrt{3}b$ supercell of an ordered Ce_2Ga_3 sheet. Similar reports of diffuse scattering along *c** with $\sqrt{3}a \times \sqrt{3}b$ supercells are found for $A_2Pt_6Al_{15}$ (A = Y, Gd−Tm, Zr),[22] $RE_{0.67}Ni_2Ga_{5+n-x}Tt_x$ (RE = Y, Sm, Gd−Tm; Tt = Si, Ge; $n = 0, 1$),[18] $Gd_{0.67}Pt_2(Al, Si)_5$, and $Gd_{1.33}Pt_3(Al, Si)_8$.[19] In $Y_2Pt_6Al_{15}$, additional streaks extending along *c** were observed at $l = 1/3, 2/3, 4/3, 5/3, 7/3, ...$, suggesting a tripled *c*-axis length.[22] In all cases, the diffraction data were interpreted to give $RE_2(M_3)$ planes in which the main-group elements compose triangles. In most cases, no stacking preferences along the *c* axis could be identified.

Our results using TEM and extended exposures of single crystals to X-ray diffraction with an image-plate detector for $RE_{1.2}Fe_4Si_{9.9}$ (RE = Gd and Y, in particular) are indicative of a periodic arrangement of RE and Si(3) atoms in the $z = 1/4$ and 3/4 planes, which differ from the $\sqrt{3}a \times \sqrt{3}b$ supercells proposed for the aluminum and gallium compounds mentioned above. TEM/HRTEM results for $Gd_{1.2}Fe_4Si_{9.9}$ and $Y_{1.2}Fe_4Si_{9.9}$ are illustrated in Figure 4. Figure 4a and b shows the HRTEM image and its corresponding selected area electron diffraction pattern (SAEDP) obtained from the [1$\bar{1}$20] orientation of $Gd_{1.2}Fe_4Si_{9.9}$. These images demonstrate that the *d* spacing is ~7.67 Å between the (0002) planes (i.e., one-half of the crystallographic *c* axis). This result is consistent with two Gd−Si(3) layers per unit cell. A 2H-layered structure is identified on the basis of the indexed SAEDP. Figure 4c and d illustrates the HRTEM image obtained along the [0001] orientation and its corresponding indexed SAEDP. This SAEDP clearly reveals strong hexagonal subcell reflections, which can be indexed with the crystallographic *a* and *b* axes with weaker but detectable superstructure reflections from a $4a \times 4b$ supercell in the crystallographic *ab* plane, as labeled by four parallel dashed lines in Figure 4d. If the pattern is indexed according to the $a \times b$ hexagonal subcell, then the superstructure reflections occur at the coordinates (*a**/4, *b**/4), (*a**/4, 2*b**/4), (2*a**/4, *b**/4), (2*a**/4, 3*b**/4), (2*a**/4, 3*b**/4), and (*a**/4, *b**/4). To the best of our knowledge, this 4-fold increase of the hexagonal *a* and *b* axes has not been observed for the other nearly isotypic compounds and could point to a different structural chemistry for the $RE_{1.2}Fe_4Si_{9.9}$ phases than for the other rare-earth/transition-metal/main-group examples

(49) Prots, Y.; Borrmann, H.; Schnelle, W.; Jeitschko, W. *Z. Anorg. Allg. Chem.* **2005**, *631*, 1218.
(50) Thiede, V. M. T.; Fehrmann, B.; Jeitschko, W. *Z. Anorg. Allg. Chem.* **1999**, *625*, 1417.

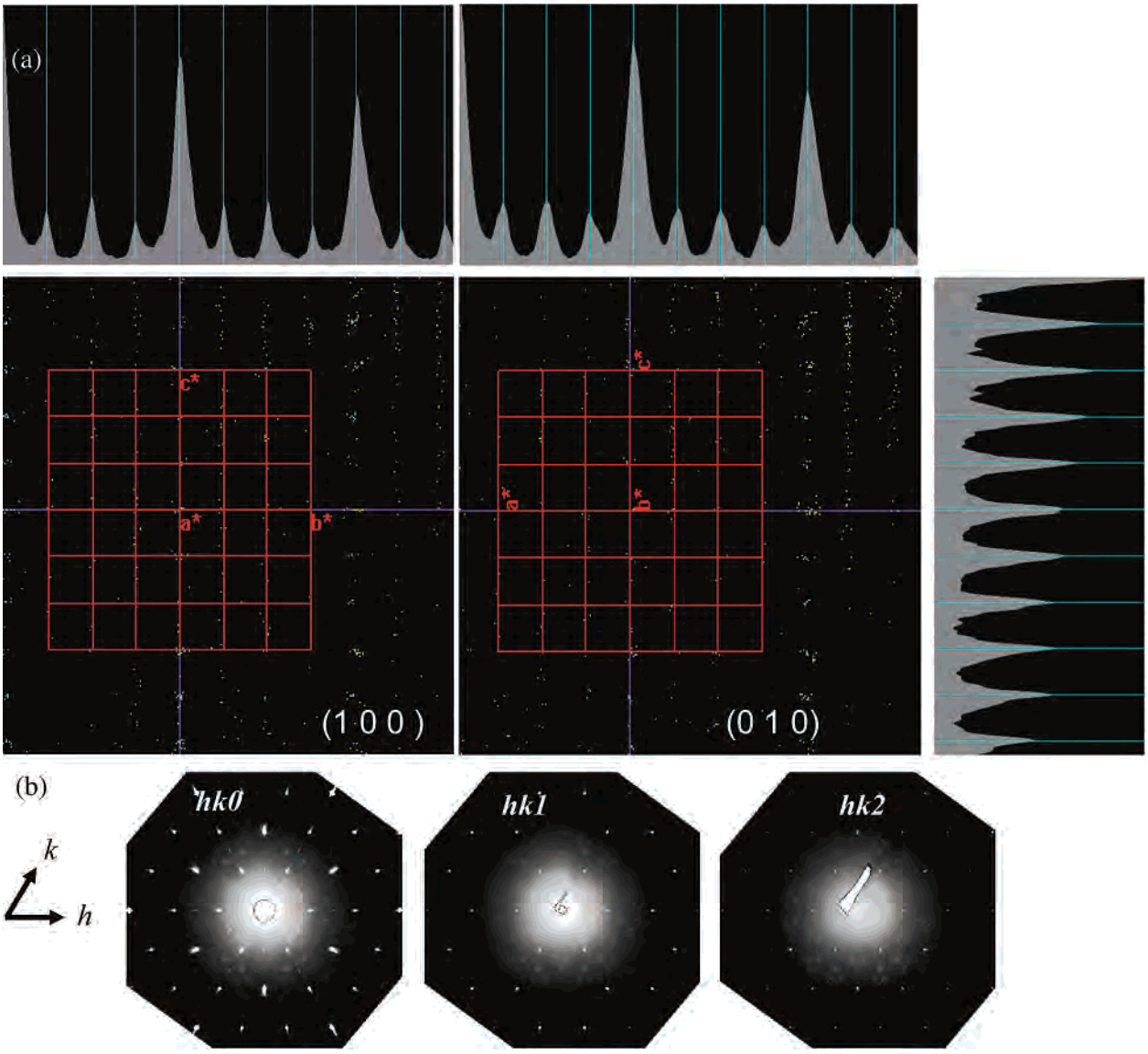

Figure 5. (a) Extended exposure diffraction images for $Gd_{1.2}Fe_4Si_{9.9}$ projected down the (left) *a** and (right) *b** directions with intensities projected along *b** (top left), *a** (top right), and *c** (far right) directions. (b) *hk*0 (left), *hk*1 (middle), and *hk*2 (right) planes of reciprocal space for $Gd_{1.2}Fe_4Si_{9.9}$ (data from STOE IPDS II).

in the literature.[16−22,46−50] Figure 4e and f shows the SAEDPs obtained, respectively, from the [11$\bar{2}$0] and [0001] orientations of $Y_{1.2}Fe_4Si_{9.9}$. A comparison of Figure 4e with b and f with d shows similar electron diffraction patterns and, therefore, similar structures for $Y_{1.2}Fe_4Si_{9.9}$ and $Gd_{1.2}Fe_4Si_{9.9}$ (i.e., a 2H-layered structure along the [11$\bar{2}$0] direction and $4a \times 4b$ supercell in the crystallographic *ab* plane). TEM characterizations on $Tb_{1.2}Fe_4Si_{9.9}$, $Dy_{1.2}Fe_4Si_{9.9}$, $Ho_{1.2}Fe_4Si_{9.9}$, $Er_{1.2}Fe_4Si_{9.9}$, $Tm_{1.2}Fe_4Si_{9.9}$, $Yb_{1.2}Fe_4Si_{9.9}$, and $Lu_{1.2}Fe_4Si_{9.9}$ samples indicate the same patterns and possible structures similar to that of $Gd_{1.2}Fe_4Si_{9.9}$ and $Y_{1.2}Fe_4Si_{9.9}$.

Figure 5a shows images along *a** and *b** from the single-crystal X-ray diffraction using a STOE image-plate diffractometer for $Gd_{1.2}Fe_4Si_{9.9}$. In both images, weak diffuse scattering is observed along the *c** axis of the reciprocal unit cell, thus indicating nonperiodic stacking of the Gd−Si(3) planes along the hexagonal *c* axis. These images do suggest the existence of a $4a \times 4b$ supercell structure because the projections of all diffraction maxima along *a** and *b** are consistent with the unusual pattern of maxima seen in electron diffraction (Figure 4d and f). To emphasize this conclusion, reciprocal space images of the *hk*0, *hk*1, and *hk*2 planes for $Gd_{1.2}Fe_4Si_{9.9}$ have been reconstructed using the *SPACE* program, shown in Figure 5b. There is no indication of twinning by pseudomerohedry because no splitting is observed for any reflection. There are also satellite reflections consistent with a $4a \times 4b$ superstructure (this is especially evident in the *hk*2 plane). The broad reflections observed in these diffraction patterns are consistent with the disorder in the structure discussed previously. However, because of the diffuse scattering, we are unable to adequately refine these data for a $4a \times 4b \times c$ unit cell. Therefore, from a combination of electron diffraction and X-ray diffraction, we conclude that the RE−Si(3) planes in $RE_{1.2}Fe_4Si_{9.9}$ adopt a $4a \times 4b$ superstructure but that these planes show stacking disorder along the *c* axis.

In an attempt to understand the observed electron and X-ray diffraction patterns and the structure leading to them

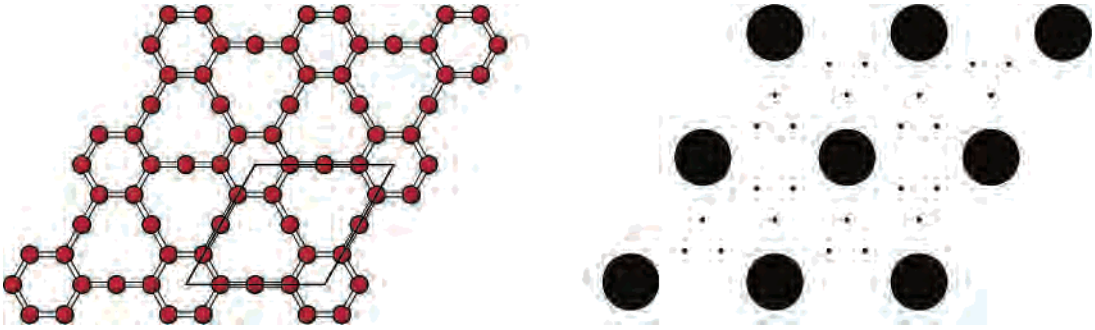

Figure 6. (left) Hexagonal plane of RE atoms forming a network with plane group *p6mm* and (right) the corresponding theoretical diffraction pattern.

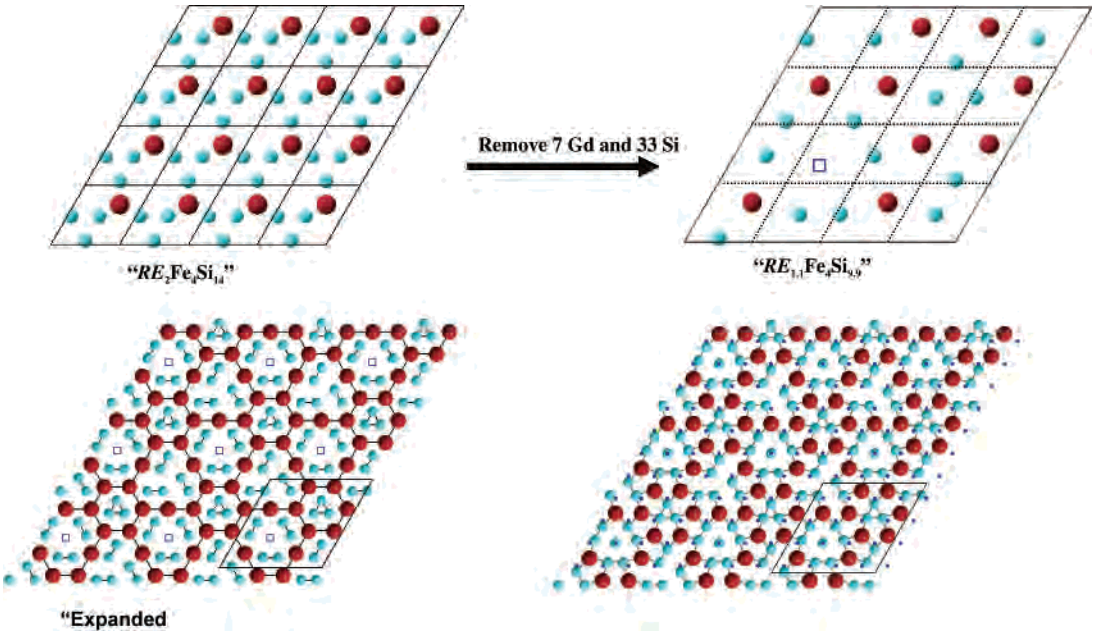

Figure 7. Construction of the superstructure in the RE/Si(3) plane at $z = 1/4$ in $RE_{1.2}Fe_4Si_{9.9}$. (top, left) The $4a \times 4b$ arrangement of crystallographic unit cells with all RE and Si(3) sites occupied. (top, right) The RE/Si(3) plane after the removal of 7 RE and 33 Si(3) atoms. Vacant site is noted by open box. (bottom, left) An expanded view of the $4a \times 4b$ RE−Si(3) superstructure to emphasize the network of RE atoms and Si(3) atoms. (bottom, right) The same expanded view together with one layer of Fe atoms in the $FeSi_2$ layers immediately below. (RE, red spheres; Fe, blue spheres; Si, light-blue spheres).

for $RE_{1.2}Fe_4Si_{9.9}$, we have constructed a two-dimensional, monatomic model structure, shown in Figure 6a. This network has plane group *p6mm* with 9 atoms in the unit cell forming a pattern of hexagons and nine-membered rings with trigonal symmetry. The theoretical 2D diffraction pattern in Figure 6b shows quite a resemblance to Figure 4d and f: the primary diffraction maxima occur at $(h, k) = (4m, 4n)$ (m, n integers), while secondary maxima with relative theoretical intensity of 1/9 the primary reflections occur at $\{(a^*/4, b^*/4), (a^*/4, 2b^*/4), (2a^*/4, b^*/4), (2a^*/4, 3b^*/4), (2a^*/4, 3b^*/4)$, and $(a^*/4, b^*/4)\} + \{(4m, 4n)\}$. These spots correspond to the observed superstructure reflections in Figure 4d and f. From this simple 2D model, we can now propose a possible superstructure model for the RE−Si(3) plane, which is illustrated in Figure 7. In each $4a \times 4b$ supercell plane, we start with 16 [$RE(Si)_3$] subcells. Then, we remove 7 RE atoms and 33 Si(3) atoms to give [RE_9Si_{15}] planes. The 9 RE atoms adopt the arrangement illustrated in Figure 6a, but the 7 open sites cannot all be replaced by $Si(3)_3$ triangles because of distance restrictions. Therefore, we propose one $Si(3)_3$ triangle inside the hexagon, but then two different sets of 3 Si(3)−Si(3) dimers within the nine-membered rings to retain the trigonal symmetry that is seen in the (0001) SAEDP images. This construction gives reasonable interatomic distances (i.e., 2.822−2.860 Å for RE−Si(3) and 2.340−2.390 Å for Si(3)−Si(3)). At this stage of the model, however, there is a significant vacancy at the center of one of the nine-membered rings: at coordinate (1/3, 2/3) in the supercell.

In the complete 3D structures of $RE_{1.2}Fe_4Si_{9.9}$, the RE−Si(3) planes occupy mirror planes. Therefore, with respect to the $FeSi_2$ layers above and below these planes, every Si(3) atom has two close Fe atoms. There are also Fe atoms, which would be separated by an approximate distance of 4.6 Å, that occupy sites above and below the vacancy position in these planes. The ratio of these two different Fe sites, based on their different local environments, is 15:1. Note that the $FeSi_2$ layers are fully occupied and well ordered. When we take into account our model for the RE−Si(3) planes and the completely ordered $FeSi_2$ layers, the $4a \times 4b \times c$ supercell contains the formula $[RE_9Si_{15}]_2[Fe_{32}Si_{64}]_2 = RE_{18}Fe_{64}Si_{158}$, which results in the composition $RE_{1.125}Fe_4Si_{9.875}$ for the hexagonal subcell and is close to the average observed compositions $RE_{1.17(1)}Fe_4Si_{9.88(4)}$ obtained

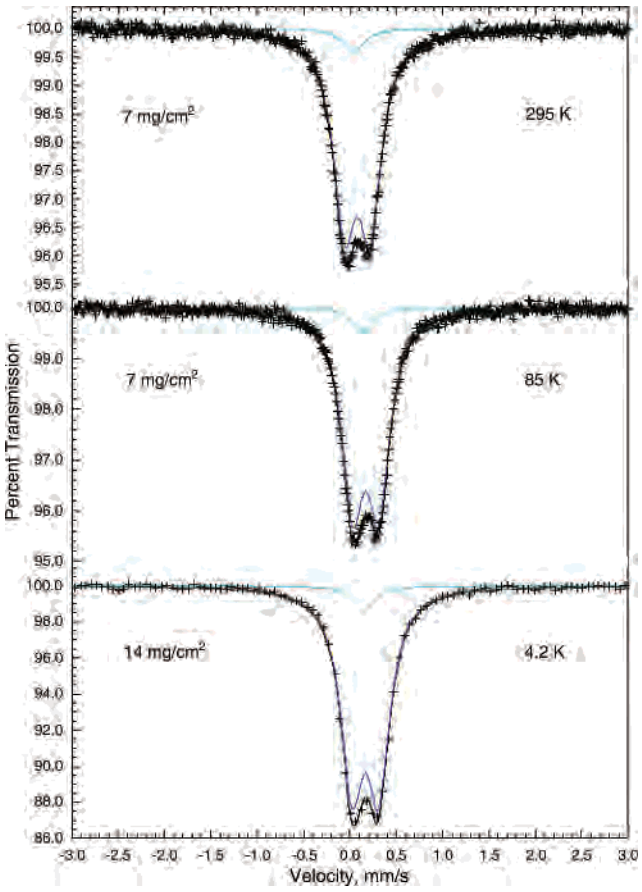

Figure 8. Mössbauer spectra of $Gd_{1.2}Fe_4Si_{9.88}$ obtained at the indicated temperatures. The majority site is shown in dark blue and the minority site in light blue.

from single-crystal structure refinements and EDS measurements. Given the diffuse scattering and the various diffraction results, we conclude that, although these layers are 7.62−7.67 Å apart, they are randomly positioned relative to each other along the *c* direction. Nevertheless, their arrangements with respect to the interspersed $FeSi_2$ slabs do yield an Fe coordination environment that is nearly regular.

Mössbauer Spectral Results. The Mössbauer spectra of all the nominal $RE_{1.2}Fe_4Si_{9.9}$ compounds have been measured at 85 and 295 K, and the spectrum of $Gd_{1.20(1)}Fe_4Si_{9.88(4)}$ has also been measured at 4.2 K. Figure 8 illustrates these spectra for $Gd_{1.20(1)}Fe_4Si_{9.88(4)}$. The Mössbauer spectra of all $RE_{1.2}Fe_4Si_{9.9}$ compounds are very similar to those shown in this figure. The Mössbauer spectrum of $Gd_{1.20(1)}Fe_4Si_{9.88(4)}$ measured at 4.2 K for ±12 mm/s also indicates that there is no long-range magnetic order, which agrees with the conclusions from magnetization and specific-heat measurements.[27]

The observed Mössbauer spectral results fully support the above proposal of a $4a \times 4b \times c$ superstructure for these compounds. All of the compounds exhibit asymmetric Mössbauer spectra, as can be seen in Figure 8, that cannot be fit with a single doublet but which require two doublets or one doublet and one singlet. It seems unlikely that the observed asymmetry could be a result of texture in the absorber because the sum of the 295 K Mössbauer spectra of $Gd_{1.20(1)}Fe_4Si_{9.88(4)}$ measured at the four orientations at the magic angle of 54.7° exhibits the same asymmetry as is shown in Figure 8. The observed asymmetry is a clear indication of the two crystallographically different iron sites in a ratio of 15:1 that are found in the $4a \times 4b$ supercell. As a consequence of the proposed supercell and the observed spectral asymmetry, the Mössbauer spectra have been fit with two symmetric doublets with an area ratio of 15:1. These fits, see Table 5, indicate that the component associated with the minority site has a zero or virtually zero quadrupole splitting at all temperatures. All attempts to fit the spectra with a single doublet, as would be expected for the subcell, are totally unacceptable.

The hyperfine parameters obtained for the $RE_{1.2}Fe_4Si_{9.9}$ compounds are all reasonable for the proposed $4a \times 4b \times c$ supercell. More specifically, the 295 K isomer shift of the majority iron sites is very similar to that observed[51] for the two iron sites in β-$FeSi_2$, both of which are structurally very similar to each other. Furthermore, the majority Fe sites in

Table 5. Mössbauer Spectral Parameters

compound	site	T^b	$\delta^{a,c}$	$\Delta E_Q{}^c$	Γ^c	area^d
$Y_{1.21(1)}Fe_4Si_{9.88(4)}$	minor	295	0.042	0.00	0.29	0.027
	major		0.068	0.28	0.29	0.399
	minor	85	0.119	0.00	0.28	0.030
	major		0.160	0.29	0.28	0.452
$Gd_{1.20(1)}Fe_4Si_{9.88(4)}$	minor	295	0.035	0.01	0.29	0.012
	major		0.077	0.27	0.29	0.181
	minor	85	0.133	0.01	0.28	0.014
	major		0.168	0.28	0.28	0.202
	minor	4.2	0.147	0.00	0.29	0.014
	major		0.167	0.29	0.29	0.216
$Tb_{1.25(1)}Fe_4Si_{9.85(5)}$	minor	295	0.040	0.00	0.30	0.018
	major		0.063	0.27	0.30	0.268
	minor	85	0.132	0.00	0.29	0.020
	major		0.162	0.28	0.29	0.299
$Dy_{1.17(1)}Fe_4Si_{9.94(4)}$	minor	295	0.030	0.00	0.30	0.014
	major		0.067	0.29	0.30	0.213
	minor	85	0.121	0.00	0.30	0.016
	major		0.157	0.29	0.30	0.242
$Ho_{1.16(1)}Fe_4Si_{9.86(4)}$	minor	295	0.030	0.00	0.30	0.009
	major		0.065	0.27	0.30	0.135
	minor	85	0.132	0.00	0.29	0.010
	major		0.156	0.28	0.29	0.148
$Er_{1.05(1)}Fe_4Si_{9.90(4)}$	minor	295	0.033	0.00	0.33	0.009
	major		0.062	0.27	0.33	0.138
	minor	85	0.123	0.00	0.33	0.011
	major		0.154	0.28	0.33	0.161
$Tm_{1.21(1)}Fe_4Si_{9.90(5)}$	minor	295	0.030	0.00	0.30	0.010
	major		0.060	0.28	0.30	0.153
	minor	85	0.130	0.00	0.29	0.012
	major		0.151	0.29	0.29	0.171
$Yb_{1.07(1)}Fe_4Si_{9.91(4)}$	minor	295	0.030	0.00	0.32	0.009
	major		0.059	0.28	0.32	0.138
	minor	85	0.130	0.00	0.32	0.011
	major		0.148	0.29	0.32	0.162
$Lu_{1.21(1)}Fe_4Si_{9.78(4)}$	minor	295	0.030	0.00	0.31	0.017
	major		0.057	0.28	0.31	0.250
	minor	85	0.120	0.00	0.29	0.019
	major		0.150	0.29	0.29	0.285

[a] The isomer shifts are given relative to room temperature α-iron foil. [b] In K. [c] In mm/s. [d] In [(%e)/(mm/s)]/mg of Fe.

(51) Schaaf, P.; Milosavljevic, M.; Dhar, S.; Bibic, N.; Lieb, K.-P.; Wölz, M.; Principi, G. *Hyperfine Interact.* **2002**, *139*−*140*, 615.

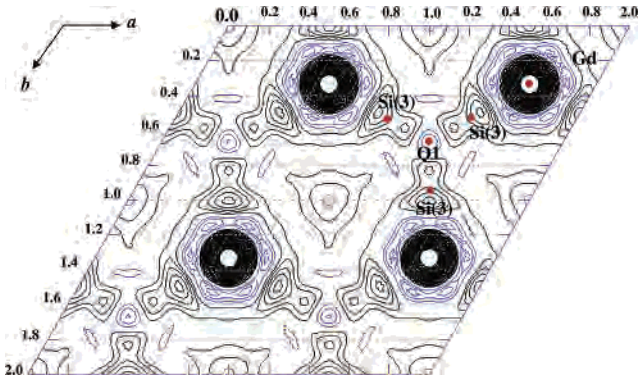

Figure 9. (001) Section of the electron density in the $z = 1/4$ plane determined by single-crystal X-ray diffraction on $Gd_{1.2}Fe_4Si_{9.88}$. Gd and Si(3) positions are marked. Q1 represents the site with the highest residual electron density from refinement of the crystallographic data.

the $RE_{1.2}Fe_4Si_{9.9}$ compounds have a 295 K quadrupole splitting that is very similar to the 0.34 mm/s splitting observed[51] for the 8*d* site in β-$FeSi_2$ but the splittings are smaller than the ~0.6 mm/s observed[51] for the 8f site in β-$FeSi_2$. Thus, it seems that the majority Fe sites in the $RE_{1.2}Fe_4Si_{9.9}$ compounds have, on average, a somewhat more symmetric electronic environment than that of the 8f site in β-$FeSi_2$, and an electronic environment that is very similar to that of the 8d site in β-$FeSi_2$.

It should also be noted that the zero or virtually zero quadrupole splitting observed in the spectra of the minority iron site in the $4a \times 4b \times c$ supercell suggests a coordination environment that is closer to a cubic arrangement than for the majority Fe sites, which have eight near-neighbor Si atoms in a distorted cubic arrangement. From this spectral observation, we conclude that the vacancy in the RE−Si(3) plane at (1/3, 2/3, 1/4) in the supercell could be occupied by a single Si atom to create a cubic coordination environment around the Fe atoms above and below this plane (the corresponding Fe−Si distance would be ~2.3 Å). To confirm this, Figure 9 shows a (001) section at $z = 1/4$ of the electron density for the subcell of $Gd_{1.20(1)}Fe_4Si_{9.88(4)}$, as determined from single crystal X-ray diffraction. The residual peak is clearly visible at the coordinate (1/3, 2/3) in the $a \times b$ subcell, and the Si(3) sites show significant distortions of their electron densities. In the $4a \times 4b$ supercell, this residual peak would occur at the coordinate (1/3, 2/3). Integration of the electron density nicely corresponds to approximately one Si atom at this site.

However, the isomer shift for the corresponding minority Fe site (Figure 10), is significantly lower than that of the majority site in the $RE_{1.2}Fe_4Si_{9.9}$ compounds and of both sites[51] in β-$FeSi_2$. This reduced isomer shift probably results because of the different atomic environments of the two Fe sites; the minority Fe site has eight near silicon and six next-near silicon neighbors but with no near RE neighbors, whereas the majority Fe sites have eight near silicon and approximately two next-near silicon neighbors and about two RE near neighbors.

A linear correlation is observed in the $RE_{1.2}Fe_4Si_{9.9}$ compounds between the isomer shifts and the unit cell volumes

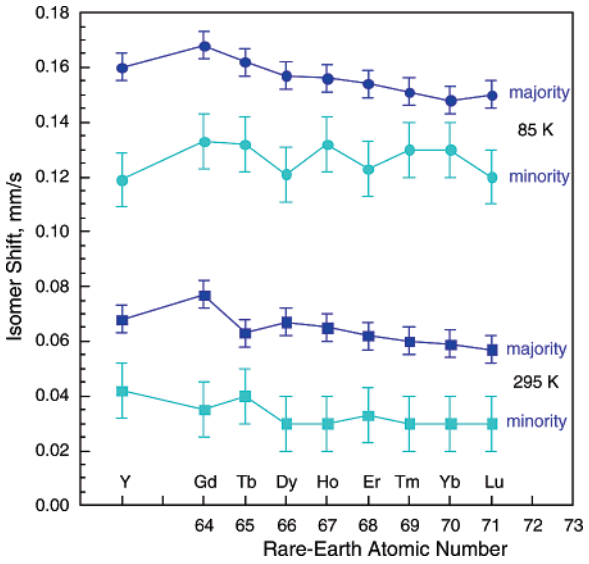

Figure 10. Variation with rare-earth element of the Mössbauer-effect isomer shift in the $R_{1.2}Fe_4Si_{10}$ compounds obtained at 85 and 295 K. The majority site is shown in dark blue and the minority site in light blue.

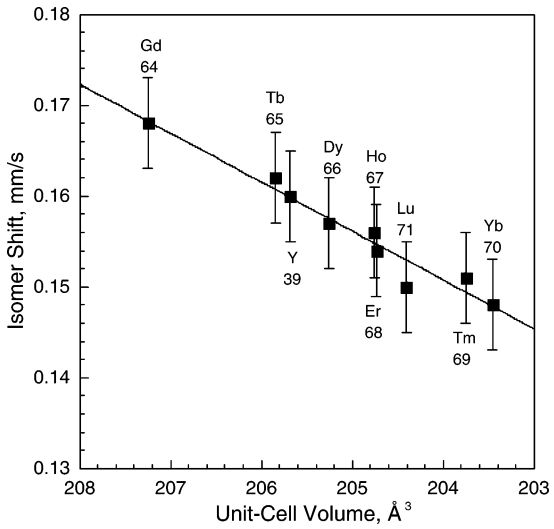

Figure 11. Correlation observed in the $RE_{1.2}Fe_4Si_{9.9}$ compounds between the 85 K Mössbauer-effect isomer shift and the unit-cell volume.

obtained from the powder X-ray diffraction results given in Tables 5 and 1. This correlation, which corresponds to the lanthanide contraction (Figure 11), indicates that as the unit cell volume decreases the s electron density at the iron-57 nucleus increases, and as expected, the isomer shift decreases with a slope of 5.38×10^{-3} (mm/s)/Å^3. This slope is rather larger than the corresponding slopes of 3.07×10^{-3} and 4.07×10^{-3} (mm/s)/Å^3 observed,[52] respectively, for the $REFe_{11}$-Ti and $REFe_{11}TiH$ series of rare-earth compounds. The volume dependence of the isomer shift in the $RE_{1.2}Fe_4Si_{9.9}$ compounds is best understood in terms of the ratio $\Delta\delta/\Delta\ln V$, previously used[53] to express the pressure dependence of the isomer shift in α-iron. This ratio is equal to 1.09, if $\Delta\delta$

(52) Piquer, C.; Grandjean, F.; Isnard, O.; Long, G. J. *J. Phys.: Condens. Mater.* **2006**, *18*, 205.
(53) Williamson, D. In *Mössbauer Isomer Shifts*; Shenoy, G. K., Wagner, F. E., Eds.; North-Holland: Amsterdam, 1978; p 317.

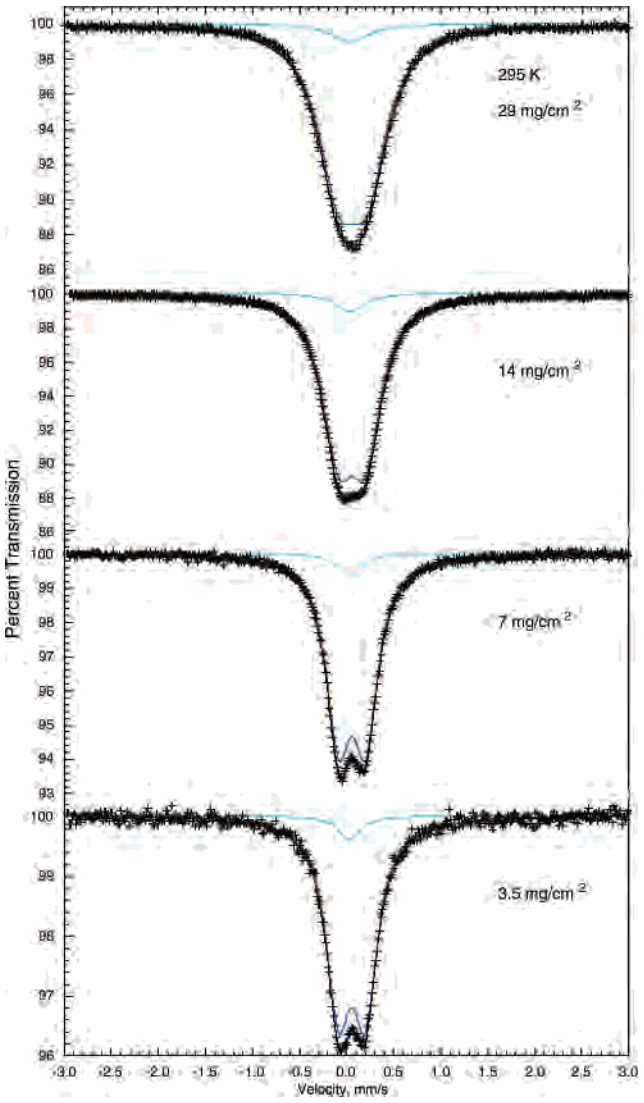

Figure 12. Mössbauer spectra of $Lu_{1.21(1)}Fe_4Si_{9.78(4)}$ obtained at 295 K at the indicated absorber thicknesses. The majority site is shown in dark blue and the minority site in light blue.

and $\Delta \ln V$ are the variation in isomer shift and in the logarithm of the unit-cell volume, respectively, between $Gd_{1.2}Fe_4Si_{9.9}$ and $Yb_{1.2}Fe_4Si_{9.9}$. This value is similar to the values[52,53] of 1.31 and 1.23 observed in α-iron and in the $REFe_{11}Ti$ compounds. The excellent linear correlation also indicates that the relative error on the isomer shift is probably smaller than 0.005 mm/s.

To detect the presence, if any, of magnetic or nonmagnetic iron-containing impurities in the $RE_{1.2}Fe_4Si_{9.9}$ compounds, preliminary spectra of each compound were measured at an absorber thickness of 29 mg/cm^2, the thickness that maximizes the signal-to-noise ratio.[54] As a consequence of this study, it was noted that the recoil-free fraction of the iron-57 nuclide in these compounds is very high and several different absorber thicknesses were used to determine the best absorber thickness. The resulting Mössbauer spectra of $Lu_{1.21(1)}Fe_4Si_{9.78(4)}$, obtained at 295 K as a function of the absorber thickness, are shown in Figure 12. This figure illustrates both the absence of any iron-containing impurity phases in $Lu_{1.21(1)}Fe_4Si_{9.78(4)}$ and the importance of using the "ideal" absorber thickness, which for $Lu_{1.21(1)}Fe_4Si_{9.78(4)}$ is between 3.5 and 7 mg/cm^2. It is immediately apparent that at higher absorber thicknesses the details of the Mössbauer spectrum are masked by the line width broadening that results from multiple γ-ray absorption processes. These studies also revealed that there was no iron component in any of the compounds that exhibits long-range magnetic order. However, 5.0, 10.4, and 4.8% spectral absorption area of a secondary iron-containing phase,[55] most likely α-$FeSi_2$, was detected in $Y_{1.21(1)}Fe_4Si_{9.88(4)}$, $Dy_{1.17(1)}Fe_4Si_{9.94(4)}$, and $Tm_{1.21(1)}Fe_4Si_{9.90(5)}$, respectively.

Table 6. Crystallographic Parameters of a Crystalline Model for $Gd_{1.2}Fe_4Si_{9.9}$[a]

atom	Wyckoff site	*x*	*y*	*z*
Gd1	6*h*	2/3	7/12	1/4
Gd2	6*h*	2/3	7/12	1/4
Gd3	6*h*	2/3	5/6	1/4
Fe1	4*f*	1/3	2/3	0.3928
Fe2	12*i*	1/6	5/6	0.6072
Fe3	12*i*	7/12	5/12	0.1072
Fe4	12*i*	1/12	11/12	0.1072
Fe5	12*i*	1/12	2/3	0.1072
Fe6	12*i*	2/3	1/12	0.8928
Si1	4*f*	1/3	2/3	0.9546
Si2	12*i*	1/6	5/6	0.0454
Si3	12*i*	11/12	1/12	0.0454
Si4	12*i*	5/12	7/12	0.0454
Si5	12*i*	5/12	1/3	0.0454
Si6	12*i*	1/3	5/12	0.9546
Si7	4*e*	0	0	0.6320
Si8	12*i*	1/2	1/2	0.8680
Si9	12*i*	3/4	1/4	0.8680
Si10	12*i*	1/4	3/4	0.8680
Si11	12*i*	1/4	0	0.8680
Si12	12*i*	0	1/4	0.1320
Si13	6*h*	0.2656	0.1328	1/4
Si14	6*h*	0.7656	0.3828	1/4
Si15	6*h*	0.0156	0.1328	1/4
Si16	6*h*	0.5156	0.6328	1/4
Si17	6*h*	0.5156	0.8828	1/4
Si18	2*c*	1/3	2/3	1/4

[a] $a' = 15.8064$ Å; $c' = 15.3421$ Å; space group = $P6_3/m$.

Structure of the $RE_{1.2}Fe_4Si_{9.9}$ Compounds Revisited. On the basif of the X-ray and electron diffraction, electron microscopy, and Mössbauer spectral analyses, we have constructed the following model for the structures of the $RE_{1.2}Fe_4Si_{9.9}$ compounds. The unit cell has at least trigonal symmetry and involves two [Fe_2Si_4] slabs alternating with two [$RE_{0.56}Si$] planes to give the final compositions, $RE_{1.12}Fe_4Si_{10}$. The iron silicide portions are well ordered, and all sites are fully occupied. The [$RE_{0.56}Si$] planes sit at mirror planes in the structure, and the arrangement of Si atoms in these planes creates two different types of Fe environments in a ratio of ~15:1. In this plane, there are three distinct types of Si atoms: (1) Si trimers, (2) Si dimers, and (3) Si atoms. To keep the majority-to-minority Fe atom ratio at ~15:1, this crystallographic model could tolerate Si vacancies

(54) Long, G. J.; Cranshaw, T. E.; Longworth, G. *Mössbauer Effect Ref. Data J.* **1983**, *6*, 42.

(55) Reuther, H.; Behr, G.; Teresiak, A. *J. Phys.: Condens. Matter* **2001**, *13*, L225.

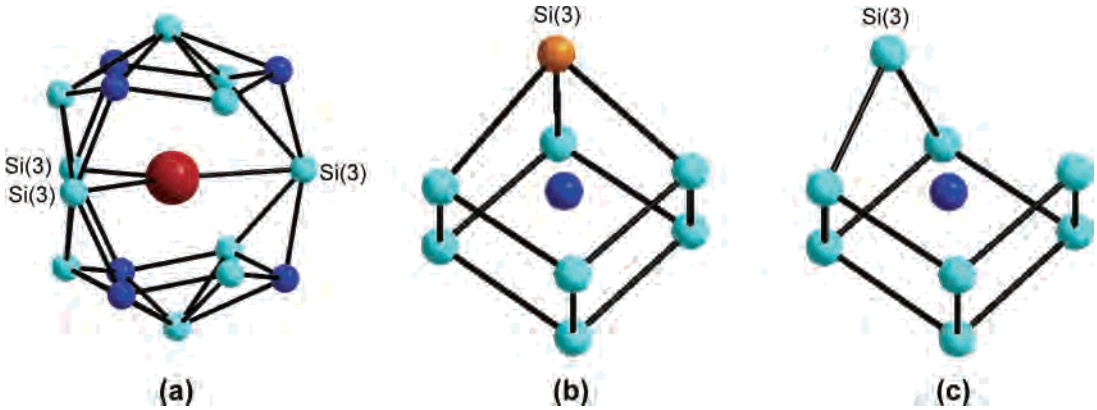

Figure 13. Local coordination environments of the (a) RE and Fe atom sites in the model superstructure of $RE_{1.2}Fe_4Si_{9.9}$ (space group $P6_3/m$). The minority Fe site is shown in b, and the majority Fe site is shown in c. (RE atom, red sphere; Fe, blue spheres; Si, light-blue spheres; Si (the Q1 site and as concluded from Mössbauer spectroscopy), tan sphere.)

in the Si-trimer sites. Such vacancies would yield the chemical formula $RE_{1.12}Fe_4Si_{10-2\delta}$, which agrees better with the chemical analysis. Although the diffuse X-ray scattering along c^* precludes an exact crystallographic solution, which includes an accurate refinement of site occupation factors, because of the random stacking arrangements of the $[RE_{0.56}Si_{1-\delta}]$, we can construct a crystallographic unit cell in an attempt to account for our observations and to illustrate the local environments for each atomic site. This model structure belongs to the space group $P6_3/m$ (No. 176) with lattice parameters of $a' = 4a$ and $c' = c$. Table 6 lists fractional coordinates for the atomic sites in this model based on $Gd_{1.20(1)}Fe_4Si_{9.88(4)}$. The composition of this model in its unit cell is $Gd_{18}Fe_{64}Si_{160}$, which is $Gd_{1.125}Fe_4Si_{10}$. Although there are six distinct Fe sites, five of them (60 atoms total) have similar coordinate environments distinct from the sixth site (4 atoms). A simulated precession pattern for this model using the *ATOMS*, version 5.0.7, program[56] gives a (*hk*0) diffraction pattern similar to the SAEDP in Figure 4d.

The RE atoms are coordinated by a pentacapped trigonal prism of 11 Si atoms with 6 Fe atoms forming another trigonal prismatic environment by bridging every edge of the Si-prismatic triangles, shown in Figure 13a. There are two general kinds of coordination environments for the Fe atoms, shown Figure 13b. Both Fe sites are surrounded by eight Si atoms in distorted cubes. These cubes share edges to create the $FeSi_2$ layers.

Physical Properties of $RE_{1.2}Fe_4Si_{9.9}$. The structural model for $RE_{1.2}Fe_4Si_{9.9}$ creates the possibility for magnetic frustration if the dominant exchange interaction between the RE sites is antiferromagnetic. The hexagonal network of RE atoms proposed in Figures 6 and 7 automatically leads to this frustration because the disorder is simply proposed to occur along the *c* axis. For this reason, magnetic measurements on these $RE_{1.2}Fe_4Si_{9.9}$ compounds are of interest. Unfortunately, previous measurements on $Er_{1.2}Fe_4Si_{9.8}$ and $Gd_{1.2}Fe_4Si_{9.8}$ found no long-range magnetic ordering down to ~4 K.[26,27] We have measured the magnetic susceptibility of these compounds from 300 K down to 1.85 K and confirm this observation for all compounds. All the compounds, except for $Y_{1.2}Fe_4Si_{9.9}$ and $Lu_{1.2}Fe_4Si_{9.9}$, follow Curie−Weiss paramagnetic behavior. The $Y_{1.2}Fe_4Si_{9.9}$ and $Lu_{1.2}Fe_4Si_{9.9}$ samples give magnetic responses $\sim 10^3$ smaller in magnitude with a small paramagnetic impurity exhibited at lower temperatures. Figure 14 shows the temperature dependence of the magnetic susceptibility and the inverse susceptibility for $Gd_{1.20(1)}Fe_4Si_{9.88(4)}$, and Table 7 summarizes the results of fitting the susceptibilities of all the $RE_{1.2}Fe_4Si_{9.9}$ compounds to a modified Curie−Weiss relation, $\chi(T) = \chi_0 + C/(T - \Theta_p)$. The temperature-independent term, χ_0, contains both the diamagnetic core contributions and a Pauli paramagnetic term. From the fits, the Pauli paramagnetic term more than cancels the diamagnetic core correction, but it also indicates a small value of the density of states at the corresponding Fermi levels. The effective magnetic moments agree well with the theoretical values for the isolated RE atom values (Yb behaves as Yb^{3+} according to these data) and suggest little contribution from Fe atoms to the magnetic responses of these compounds, as is the case in β-$FeSi_2$, which is a diamagnetic semiconductor. The Weiss constants range between −12 K for Gd and +35.9 K for Yb, to suggest very weak (essentially no) magnetic exchange coupling between rare-earth elements down to ~2 K.

Figure 14 also shows the temperature dependence of the resistivity for a polycrystalline sample of $Gd_{1.20(1)}Fe_4Si_{9.88(4)}$. Resistivity measurements indicate poor metallic behavior with a large residual resistivity at low temperatures, which is attributed to the intrinsically disordered structure.

Electronic Structure and Structure/Bonding Relationships. To elucidate possible chemical bonding features influencing the stability of $RE_{1.2}Fe_4Si_{9.9}$, preliminary TB-LMTO-ASA electronic-structure calculations of the electronic densities of states (DOS) were performed on three structure models with RE = Y: (a) a hexagonal "$Y_2Fe_4Si_8$" = $[Y(Si)_0]_2[Fe_2Si_4]_2$, (b) a monoclinic "YFe_4Si_{10}" = $Y_2Fe_8Si_{20}$ = $[Y(Si)_2]_2[Fe_4Si_8]_2$, and (c) an orthorhombic "$Y_2Fe_6Si_{15}$" = $Y_4Fe_{12}Si_{30}$ = $[Y_2(Si)_3]_2[Fe_6Si_{12}]_2$. In each of these models, the $FeSi_2$ layers are identical, whereas the Y−Si planes differ: (a) inYFe_4Si_{10},

(56) Dowty, E. *ATOMS*, version 5.0.7; Shape Software, Kingsport, TN.
(57) Giedigkeit, R.; Schnelle, W.; Grin, Yu.; Jeitschko, W. *Collected Abstracts of VIIth European Conference on Solid State Chemistry*; Madrid, Spain, 1999; p 136.

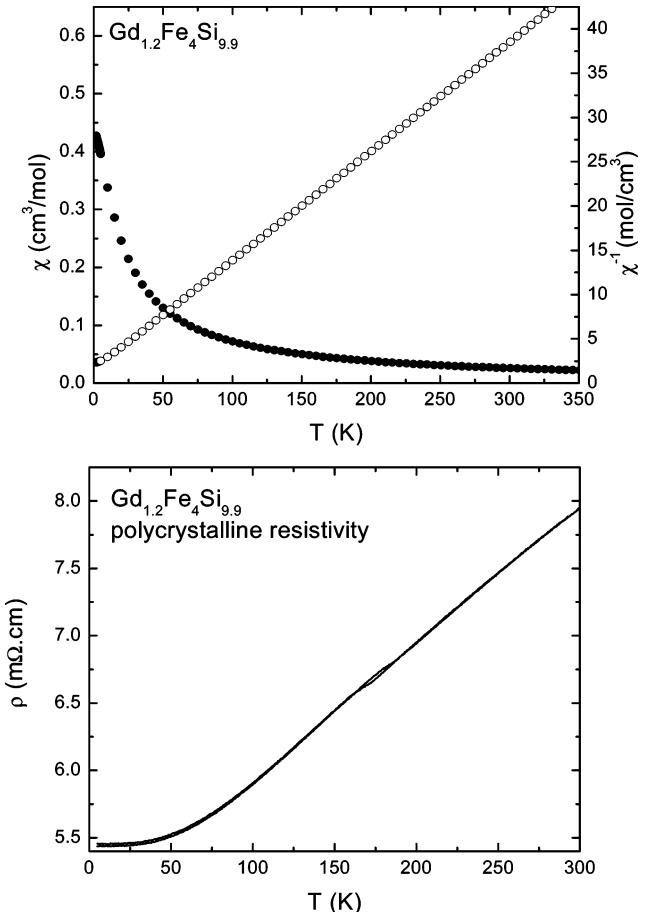

Figure 14. (top) Temperature dependence of the magnetic susceptibility and the inverse susceptibility of a $Gd_{1.20(1)}Fe_4Si_{9.88(4)}$ polycrystalline sample. (bottom) Temperature dependence of the resistivity of the $Gd_{1.20(1)}Fe_4Si_{9.88(4)}$ polycrystalline sample.

Table 7. Magnetic Properties of $RE_{1.2}Fe_4Si_{9.9}$ Compounds as Determined from Numerical Fits of Magnetic Susceptibilities to a Modified Curie−Weiss Relation, $\chi(T) = \chi_0 + C/(T - \Theta_p)$

RE	χ_0 (emu/mol)	μ_{eff} (μ_B/*RE*)	μ_{free} (μ_B)	Θ_p (K)
Y		0	0	
Gd	0.0002(1)	8.1(1)	7.94	−12(1)
Tb	0.0028(2)	9.62(1)	9.72	0.3(1)
Dy	0.0043(2)	9.89(1)	10.65	1.5(1)
Ho	0.00184(7)	10.81(1)	10.61	14.8(3)
Er	0.0083(7)	9.34(1)	9.58	4.2(2)
Tm	0.0004(1)	8.06(1)	7.57	0.1(1)
Yb	0.0062(1)	4.56(1)	4.54	35.9(5)
Lu		0	0	

the Y sites are fully occupied and the Si sites are empty; (b) in YFe_4Si_{10}, 1/2 of the Y sites and 1/2 of the Si-trimer sites, occupied by a factor 2/3 to give only Si−Si dimers, are occupied; and (c) in $Y_2Fe_6Si_{15}$, 2/3 of the Y sites and 1/3 of the Si-trimer sites are occupied. The corresponding DOS curves are compared with the calculated DOS for semiconducting β-$FeSi_2$ in Figure 15. All of the ternary structures show a pseudogap in their DOS curves for a valence electron count of ~38 electrons per $Y_mFe_2Si_n$ (i.e., per two Fe atoms in the chemical formula) and have general features consistent with the DOS curve of β-$FeSi_2$. States in the pseudogap regions arise from orbital contributions of all atoms, with states just below the pseudogap arising largely from Fe 3d

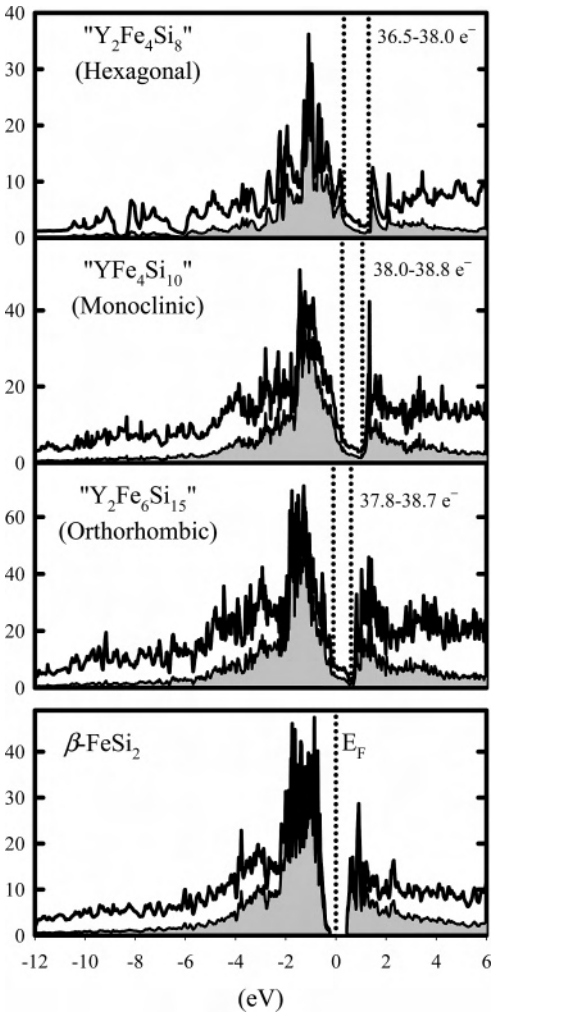

Figure 15. Total DOS curves and projections of Fe orbitals for hexagonal $Y_2Fe_4Si_8$, monoclinic YFe_4Si_{10}, and orthorhombic $Y_2Fe_6Si_{15}$ compared to the DOS curve for β-$FeSi_2$. The Fermi level for β-$FeSi_2$ is marked by the dotted line. For the various model structures, the dotted lines indicate the pseudogap range and the numbers of valence electrons required to fill states to that energy range is given for each case.

orbitals mixing with Si 3p orbitals. The valence electron counts associated with each of the model structures do not correspond exactly with the values assigned by chemical analysis or refinement of X-ray diffraction data, so we hypothesize that the chemical compositions are adjusted to achieve Fermi levels in these pseudogap regions. A more thorough analysis of the electronic structures for these and related systems is in progress. Nevertheless, the existence of a pseudogap in the DOS for this $RE_{1.2}Fe_4Si_{9.9}$ system is consistent with both the low Pauli paramagnetic susceptibility and the poor metallic character of these materials.

The nearly identical valence electron counts assigned to the location of the pseudogap in the three Y−Fe−Si model structures strongly indicate chemical-bonding driving forces for both stabilizing this class of structures and, probably, influencing the superstructure behavior. As we have mentioned, this $RE_{1.2}Fe_4Si_{9.9}$ class of compounds is part of a growing class of rare-earth (R)/transition-metal (T)/main-group element (M) structures showing similar features: (1) fluorite-type TM_2 layers alternating with intrinsically disordered or ordered $R_x(M_{3-y})_{1-x}$ planes with a hexagonal subcell,

Table 8. Summary of R−T−M Crystal Structures Related to $RE_{1.2}Fe_4Si_{9.9}$ Compounds Including the Stacking Sequence, Valence Electron Counts, and Space-Group Symmetries[a]

compound	space group	formula for hexagonal subcell	−[R−M]-[TM_2]− stacking	valence-electron count	ref
$Y_2Co_3Ga_9$	*Cmcm*	$Y_{0.67}CoGa_3$	−[$Y_2(Ga_3)$][c]-[Co_3Ga_6][e]−	20	48
$Yb_2Pd_3Ga_9$	*P*6$_1$22	$Yb_{0.67}PdGa_3$	−[$Yb_2(Ga_3)$][c]-[Pd_3Ga_6][e]−	21	57
$Y_3Ru_{4.06}Al_{11.94}$	*P*6$_3$/*mmc*	$Y_{0.75}Ru_{1.01}Al_{2.99}$	−[$Y_3(Al_{2.94}Ru_{0.06})Al$][d]-[$Ru_4Al_8$][e]−	19.3	17
$Gd_3Os_{4.44}Al_{11.56}$		$Gd_{0.75}Os_{1.11}Al_{2.89}$	−[$Gd_3(Al_{2.68}Os_{0.32})Al$][d]-[$Os_{4.12}Al_{7.88}$][e]−	19.8	17
$Gd_{0.67}Pt_2Al_5$	*P*6$_3$/*mmc*	$Gd_{0.67}Pt_2Al_5$	−[$Gd_{0.67}(Al_3)_{0.33}$][b]-[Pt_2Al_4][f]−	37	19
$Gd_{0.67}Pt_2Al_4Si$		$Gd_{0.67}Pt_2Al_4Si$	−[$Gd_{0.67}(M_3)_{0.33}$][b]-[Pt_2M_4][f]−	38	19
$Ce_{1.28}Pt_4Ga_{9.88}$		$Ce_{0.64}Pt_2Ga_{4.94}$	−[$Ce_{0.64}(Ga_3)_{0.31}$][b]-[Pt_2Ga_4][f]−	36.74	46
$Y_{1.36}Pt_4Al_{9.92}$		$Y_{0.68}Pt_2Al_{4.96}$	−[$Y_{0.68}(Al_3)_{0.32}$][b]-[Pt_2Al_4][f]−	36.92	22
$Zr_{1.00}Pt_4Al_{10.22}$		$Zr_{0.50}Pt_2Al_{5.11}$	−[$Zr_{0.50}(Al_3)_{0.37}$][b]-[Pt_2Al_4][f]−	37.33	22
$Y_{0.67}Ni_2Ga_{4.33}Ge_{0.67}$		$Y_{0.67}Ni_2Ga_{4.33}Ge_{0.67}$	−[$Y_{0.67}(Ga_3)_{0.33}$][b]-[Ni_2M_4][f]−	37.67	18
$Y_{1.2}Fe_4Si_{9.9}$		$Y_{0.6}Fe_2Si_{4.5}$	−[$Y_{0.6}(Si_3)_{0.31}$][b]-[Fe_2Si_4][f]−	37.6	this work
$Gd_{1.33}Pt_3Al_8$	$R\bar{3}m$	$Gd_{1.33}Pt_3Al_8$	−[$Gd_{0.67}(Al_3)_{0.33}$][b]-[$PtAl_2$][e]-[$Gd_{0.67}(Al_3)_{0.33}$][b]-[Pt_2Al_4][f]−	58	19
$Gd_{1.33}Pt_3Al_7Si$	$P\bar{1}$	$Gd_{1.33}Pt_3Al_7Si$		59	19
$R_4Pt_9Al_{24}$		$R_{1.33}Pt_3Al_8$	−[$Gd_{0.67}(M_3)_{0.33}$][b]-[PtM_2][e]-[$Gd_{0.67}(M_3)_{0.33}$][b]-[Pt_2M_4][f]−	58	50
$R_4Pd_9Al_{24}$		$R_{1.33}Pd_3Al_8$	−[$R_2(Al_3)$][c]-[Pd_3Al_6][e]-[$R_2(Al_3)$][b]-[Pd_6Al_{12}][f]−	58	50

[a] The valence-electron count is based on the (hypothetical) hexagonal subcell formula. The various [R−M] and [TM_2] compounds are illustrated in the following footnotes as indicated by superscripts in the stacking description.

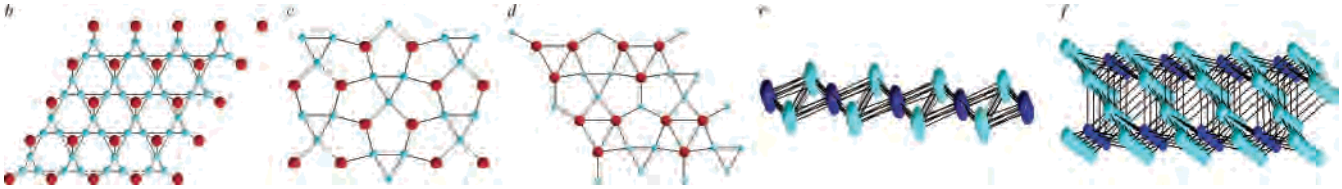

as observed for $RE_{1.2}Fe_4Si_{9.9}$; (2) the transition metals are exclusively from groups 8−10; and (3) the main-group elements remain limited to Al, Ga, Si and Ge. The TM_2 layers are (111) sections cut from the fluorite-type TM_2 framework. Also, the $R_x(M_{3-y})_{1-x}$ composition of the planes both represents the structural motif that either a rare-earth element or a M_3 triangle adopts at or around a single crystallographic site in the hexagonal subcell and indicates that the M_3 triangle does tolerate vacancies.

Table 8 lists a selection of those compounds that have a close relationship to the $RE_{1.2}Fe_4Si_{9.9}$ compounds. We express the compositions according to both the literature and the hexagonal subcell; for the ordered triclinic or orthorhombic structures, such a subcell is indeed hypothetical. For all reported structures so far, only two (001) sections from the fluorite structure type have been observed: (i) one TM_2 layer or (ii) two adjacent TM_2 layers (designated as T_2M_4 in Table 8). The single TM_2 can be described as a distorted CdI_2-type layer, but we believe there is a stronger relationship to the fluorite-type arrangement and prefer this alternative description. From the valence-electron concentrations listed, there is a clear electron-counting rule for these compounds. For compounds built from single TM_2 layers, we find ∼19−20 valence electrons; for compounds built from double TM_2 layers, we find ∼37−38 valence electrons, and for those involving an equal mixture of the two layer types, we find ∼58 valence electrons, the sum of the two separate valence electron counts. The TM_2 groups forming these structures have 14−16 valence electrons per formula unit, and all of the T elements involved, except perhaps Fe, have low-lying valence d orbitals, so these would be formally filled in the DOS (note that through strong Fe−Si orbital overlap, we can essentially assign the Fe 3d band as "filled", but this "ionic" picture is highly misleading). This electronic assignment means that the RE−M planes must contribute ∼4−6 valence electrons per plane. Further assessment of this valence electron-counting rule is needed, and theoretical studies are presently underway.

Summary

We have synthesized and characterized a series of ternary rare-earth iron silicides, $RE_{1.2}Fe_4Si_{9.9}$ (RE = Y, Gd−Lu), and have demonstrated a new superstructure for this class of rare-earth/transition-metal/main-group element compound. The structures involve (111) sections cut from fluorite-type TM_2 structures alternating with R−M planes that typically show intrinsic disorder within a hexagonal subcell on the basis of interatomic distances. A combination of TEM, X-ray diffraction, and Fe Mössbauer spectroscopy helped to characterize their structures. Magnetic measurements revealed no significant magnetic exchange, and all the compounds are poor metallic conductors. Preliminary electronic-structure calculations indicate pseudogaps in the DOS curves of model structures of $RE_{1.2}Fe_4Si_{9.9}$ and suggest an electron-counting rule for such compounds. A survey of various R−T−M examples confirmed this preliminary conclusion and is leading to further theoretical and experimental investigations of these systems.

Acknowledgment. This work was supported by NSF DMR 02-41092. F.G. acknowledges the financial support of the Fonds National de la Recherche Scientifique for Grant 9.456595. The authors are grateful to Dr. Alfred Kracher for the Energy-Dispersive X-ray Spectroscopy measurements, to Dr. Yuri Janssen for magnetization measurements, and to Dr. R. P. Hermann and Ms. L. Rebbouh for their help in the

Mössbauer spectroscopy laboratory. The electron-beam analyses were performed at the Ames Laboratory, which is operated for the U.S. Department of Energy by Iowa State University under Contract W-7405-Eng-82. G.M. also wishes to thank Prof. Yuri Grin at the Max-Planck-Institute for Chemical Physics of Solids in Dresden, Germany for providing resources to help complete this work.

Supporting Information Available: X-ray crystallographic files in CIF format for the structure determinations of $RE_{1.2}Fe_4Si_{9.9}$ (RE = Y, Gd−Lu) and plots showing the temperature dependences of the magnetization susceptibilities and inverse susceptibilities. This material is available free of charge via the Internet at http://pubs.acs.org.

IC061117C